University of Canterbury
School of Physical and Chemical Sciences

Membership and seismic analysis of red giants in open clusters

A study on M67, Ruprecht 147 and NGC 2158

Ruchita Malpathak

Supervisors: Dr Karen Pollard[1] and Dr Anna F McLeod[2,3]

A thesis presented for the degree of Master of Science

November 2019

[1]University of Canterbury, Christchurch
[2]University of California, Berkeley
[3]Texas Tech University, Lubbock

"Study hard what interests you the most in the most undisciplined, irreverent and original manner possible."

-Richard Feynman

Abstract

Star clusters form via the gravitational collapse of molecular clouds, hence the stars they contain are dynamically linked. Stellar clusters provide an insight into star formation, an important question in astrophysics, as most stars are formed in this environment. The initial conditions of a star-forming region determines the evolution of the stars. Observations show that the angular momentum of the cloud while forming stars is disturbed by turbulence. Recent studies show that the alignment of the inclination angles of stars' spin axis - relative to our line of sight - in an open cluster is evidence that the signature of turbulence of the cloud from which they formed has been retained. Red giants are bright stars which can be easily observed and hence make an excellent target for such studies. The aim of this project was to analyse the stellar populations of three open clusters in the Milky Way and to link these to the initial conditions of the molecular cloud they originally formed from using asteroseimological analysis. For the population analysis of the clusters, we use data from the Gaia mission to compute the probability for each star, if the probability is greater than two standard deviations (2σ), that star is said to be a member of the respective cluster. We select three clusters; M67, Ruprecht 147 and NGC 2158, all are more than one gigayear old and red giant rich. We find that M67 has 540 members with 29 red giants, Ruprecht 147 has 96 members with 7 red giants and NGC 2158 has 338 members with 11 red giants. With data from the *Kepler* space telescope, an asteroseismological analysis of the light curves of red giants in the old open clusters was performed. The light curves were processed using two different methods. Method A consisted manually removing trends and background contamination and Method B used the flux provided by the *Kepler* pipeline. We find that the frequency resolution for the second *Kepler* mission (K2) does not have the frequency resolution to identify individual oscillation modes, due to its loss of fine pointing. This means that the inclination angles for these cluster cannot be determined using K2 data. We conclude that M67 and R147 are excellent candidates to study star formation as they are relatively close and are red giant rich.

Declaration

Acknowledgements

I would like to sincerely thank Aai and Hansa, thank you for your constant support through all my choices and I hope that I can come through on everything you hope for me.

I would also like to thank Anna, not only for your supervision for this thesis but also for being a great mentor and helping me develop professionally.

Cheers Nick and Alejandra for the all the chats, dinners and desserts. Thank you Rosemary, for the great yarns and the 547 comments. Thank you Dylan for all your help with my silly questions. Also a thanks to Cliff, for your words of "encouragement", chats and keeping me on track for writing.

Finally, thank you Jo and Iain, for being my family and support in Christchurch and to all my friends who have made a home away from home for me.

Contents

Abstract iii

Declaration iv

Acknowledgements v

1 Introduction 1

1.1 Star formation processes . . . 2

1.1.1 Molecular cloud composition . . . 2

1.1.2 Physical mechanisms and processes . . . 3

1.1.3 Stellar evolution . . . 5

1.1.4 Star Clusters . . . 8

1.2 Asteroseismology . . . 9

1.2.1 Solar-like oscillations . . . 12

1.3 Inclination angles . . . 16

1.4 Data and telescopes . . . 18

1.4.1 Kepler and the K2 Mission . . . 18

1.4.2 Gaia . . . 20

2 Clusters 22

2.1 Cluster selection . . . 22

2.2 Cluster Membership . . . 24

2.2.1 Gaia data, astrometry and errors . . . 25

2.2.2 Cluster Membership Results: M67 . . . 35

2.2.3 Cluster Membership Results: Ruprecht 147 . . . 39

2.2.4 Cluster Membership Results: NGC 2158 43
2.2.5 Resulting RGs 47

3 Asteroseismology **49**
3.1 Light curves and reduction 49
3.1.1 Method A: SAP flux light curves 50
3.1.2 Method B: PDC flux light curves 54
3.1.3 Self-Flat Fielding 55
3.2 Peak bagging 57
3.3 Resulting parameters 66

4 Conclusion **73**

List of Figures

1.1 Hertzsprung-Russell diagram and evolutionary track 7
1.2 Doppler maps of radial velocities on a non-radial oscillator 11
1.3 Power spectra of two red giants 14
1.4 Kepler's second light: How K2 will work 19
1.5 Gaia payload 21

2.1 Unit error weight 28
2.2 Sigma clipping of proper motions 30
2.3 Gaussian fittings of distances for each cluster 33
2.4 Colour-Magnitude diagrams of M67 37
2.5 Colour-Magnitude diagrams of M67 as computed by Gaia archives . . 38
2.6 Radial profile of M67 with Kings parameters fittings 39
2.7 Colour-Magnitude diagrams of R147 41
2.8 Colour-Magnitude diagrams of R147 as computed by Curtis et al. [2013] 42
2.9 Radial profile of R147 with Kings parameters fittings 43
2.10 Colour-Magnitude diagrams of NGC 2158 45
2.11 Colour-Magnitude diagram of NGC 2158 as computed by Christian et al. [1985] 46
2.12 Radial profile of NGC 2158 with Kings parameters fittings 46

3.1 Target pixel files showing different masks 51
3.2 Unprocessed light curve, common CBV trends and de-trended light curve for 211413623 53
3.3 Unprocessed light curve from Method B 55
3.4 SFF corrected light curve for 211413623 for Method A and B 57

3.5 Periodogram for 211413623, for Methods A and B 59
3.6 Smoothed periodogram for 211413623, for both Methods A and B . . . 61
3.7 Flattened periodograms for 211413623 for Methods A and B 62
3.8 ν_{max} diagnostics showing auto-correlation function 64
3.9 $\Delta\nu$ diagnostic diagram 65
3.10 Échelle diagram examples 66

List of Tables

2.1 Cluster parameters from Kharchenko et al. [2013] 23
2.2 Cluster parameters for final target clusters 24
2.3 Gaia data which was downloaded for target clusters 26
2.4 Mean distances of each cluster 32
2.5 Cluster properties of M67 35
2.6 Cluster properties of Ruprecht 147 40
2.7 Cluster properties of NGC 2158 44
2.8 Final red giants for M67 48
2.9 Final red giants for R147 48

3.1 Parameters estimated for each star in M67 (Method A) 68
3.2 Parameters estimated for each star in M67 (Method B) 69
3.3 Parameters estimated for each star in M67 as calculated by Stello et al. [2016] 70
3.4 Parameters estimated for each star in R147 (Method A) 71
3.5 Parameters estimated for each star in R147 (Method B) 71

Chapter 1

Introduction

Stars are fundamental elements of the known universe. Hence, understanding their formation and evolution has been an important part of astronomy as it acts as a link to the evolution of the universe. It has long been accepted that stars form from the gravitational collapse of molecular clouds in the interstellar medium. This view dates back to as early as 1692 when Newton mentioned in a letter of how interstellar matter may be affected by gravity *"... the matter on the outside of this space would by its gravity tend towards all the matter on the inside, and by consequence fall down into the middle of the whole space, and there compose one great spherical mass... And thus might the sun and fixed stars be formed, supposing the matter were of a lucid nature"* [Jeans, 1929]. In the last couple of decades, with aid of technology which allowed us to observe various wavelengths, we have begun to grasp that star formation involves many physical processes which take place on multiple scales and are important to different mechanisms at different levels. On small scales, the balancing of thermal pressure against gravity is the most significant factor which determines whether star formation occurs or not. On large scales, star formation is affected by numerous factors; dissipation of turbulence, scattering of magnetic fields which form giant molecular clouds, and galactic tidal forces which form the interstellar matter [Larson, 2003].

The aim of this thesis was to investigate cluster membership of open clusters and analyse red giants to obtain asteroseismic parameters. This study is a preparatory step in using asteroseismology to study star formation. Publications such as Corsaro et al.

[2017] (a letter published in Nature in 2017; hereafter referred to as C2017), and Gizon and Solanki [2003] have already demonstrated that asteroseismology is a powerful tool in obtaining stellar parameters and understanding the internal structures of stars. C2017 stated that stars which have formed in open clusters have retained the signatures of turbulence and angular momentum of the cloud from which they formed [Corsaro et al., 2017]. They used asteroseismological techniques to analyse the inclination angles of spin axes of 48 stars in 2 open clusters. They found 70% of stars in each cluster have a strong level of alignment. Using this background we study three open clusters; M67, Ruprecht 147 and NGC 2158. The analysis begins by determining appropriate target, cluster membership and then the number of red giants in the open clusters. The asteroseismic analysis is used to find fundamental stellar properties such as mass, radius and the surface gravity of the red giants.

Section 1.1 discusses various components of star formation, including; the chemical composition of gas from which these stars form, physical mechanisms which affect the star forming rate; evolution and clustering. Cluster membership methods are based on Kharchenko et al. [2012] (a catalogue of open clusters), which along with target selection is discussed in Chapter 2. Detailed methods of asteroseismic analysis are explained in Chapter 3. Chapter 4 concludes and summarises this study.

1.1 Star formation processes

1.1.1 Molecular cloud composition

Molecular clouds are a type of interstellar cloud made up of gas and dust. These objects can either reflect or absorb the emission from stars in their vicinity. The high densities (100 - 300 molecules/per cm^3) and low temperatures (7 - 15 K) of the region mean that the gases begin clumping together [John, 2009]. Elements in molecular clouds are most commonly hydrogen (H), helium (He) and carbon (C); where 90% of the total mass is H, 10% He, 0.01% C and 0.001% is comprised of other molecules. Molecular clouds are dense, making it difficult for optical light to emerge from them; hence most observations are done at various wavelengths such as the infrared, whose

longer wavelengths that can pass through dense regions [John, 2009].

Recent studies show that galaxies similar to the Milky Way host the majority of their star formation in their spiral arms, which contain numerous giant molecular clouds (GMCs). Internal structures of GMCs contain small dense pockets approximately the size of 0.1 parsecs, which form small multi-star systems or individual stars of approximately 1 solar mass one ($M_{\odot}$). In addition, massive regions thousands of parsecs across form star clusters of a few thousand $M_{\odot}$ [Lada and Kylafis, 2012a]. Such regions are generally active star-forming regions. Molecular clouds have short lifetimes once stars begin to form; a GMC has an average lifetime of approximately 10 million years [Larson, 2003] and subsequently smaller clouds are expected to have much lower lifetimes. After stars have formed, the excess interstellar gas disbands as a result of stellar feedback produced by gas ionisation and multiple other mechanisms [Matzner, 2002]. The unevolved chemical composition of these clouds indicate their short lifetimes. Additionally, numerical simulations of turbulence support the short lifetime theory as the results show that these clouds cannot sustain against gravity [Ballesteros-Paredes et al., 2003]. At larger scales, gravitational instability is the result of stellar feedback mechanisms. The multi-kiloparsec scale of GMCs suggests that they should form primarily in the spiral arms, which is confirmed by observations [Ballesteros-Paredes et al., 2006].

1.1.2 Physical mechanisms and processes

This section presents the possible mechanisms which initiate the star forming process by generating clumps or triggering fragmentation of the molecular clouds. There are two major principles with various mechanisms: the first scenario, these clumps begin with small fluctuations in density of the molecular clouds which increase by mass accretion; and in the second scenario, fragmentation occurs as a result of supersonic turbulence and shocks which compress the gas into smaller regions. Each mechanism is discussed separately for clarity.

Gravitation

Classic theory dictates that star formation is initiated when there is a small density perturbation - which is either triggered or a results from turbulence - in an otherwise uniform molecular gas cloud. The first model for this theory was made by James Jeans. The model showed that if a molecular cloud exceeds a critical mass (classified as the Jeans mass) it undergoes gravitational collapse [Jeans, 1929]. This model has been highly criticised for having mathematical inconsistencies [Larson, 2003]. Multiple other attempts have been made in making similar models; all confirm that the Jeans mass is a valid approximation for critical mass. Once this gravitational collapse begins, a protostar - stellar object with very little mass - starts to form and grows by accreting more mass.

Rotation

Observations confirm the majority of star forming regions rotate as an expected result of turbulence. For the angular momentum to be conserved, rotation must strongly influence the later stages of molecular cloud collapse. The 'classical angular momentum problem' in star formation is that angular momentum is too strong in pre-stellar clouds when compared to that of a star. This must mean that angular momentum is lost or redistributed. The early hypothesis for this problem was that the excess angular moment comes from galactic rotation. However, there is a difference of many magnitudes and the rotation rate of pre-stellar clouds would have to be much higher than what is observed [Larson, 2003]. An explanation for this discrepancy is that during the early, low density stage the magnetic field has already carried away most of the angular momentum as the field is strongly coupled to the gas [Lada and Kylafis, 2012b]. Observations show that the measured angular momentum in the gas cloud is approximately three magnitudes larger than an individual star. The magnetic field dissipates some of this momentum; however, as it decouples at later stages, it cannot carry away all of the excess angular momentum. If the cloud is collapsing with rotation it is likely to result in the formation of binaries or multiple-star systems. This model of cloud collapse via rotation results in an accretion disk model which requires axis symmetry and is only relevant in cases where the disk does not gain enough mass to

become self gravitating [Larson, 2003]. Adding rotation to models means matter does not fall into the central protostar, but instead settles centrifugally into supported disks around the protostars.

Turbulence

Molecular clouds have irregular shapes and complex motions within them. Apart from small dense regions, these motions are supersonic, exceeding the speed of sound by 0.2 km s^{-1} [Dickman and Kleiner, 1985, Myers, 1983, Larson, 1981]. Molecular clouds have complex, broad emission lines, which show there is random motion present at small scales, as the motions at large scales (such as cloud rotation) are not significant enough to affect emission line width. Behaviour of this 'turbulence' is currently unknown and it may not be similar to classical turbulence [Larson, 1981]. Supersonic turbulence may be a significant factor since supersonic motions can generate shocks which in turn generate large density fluctuations [McKee and Ostriker, 2007]. Large scale motions show that the correlation between velocity dispersion and region size extends to the galactic scale, which implies that turbulence at small scales is part of larger scale system of interstellar turbulence [Larson, 2003]. While the workings of large scale turbulence are not well understood, there are multiple mechanisms which affect it and these might differ depending on regions. Known sources which affect large scale motions include stellar feedback and gravitation.

1.1.3 Stellar evolution

All stars begin as a protostar, however the rest of its evolution is determined by how much masses the protostar has accumulated. Stars which have mass of 0.012 $M_\odot$ to 0.8 $M_\odot$ are known as brown dwarfs and do not reach high enough temperatures to fuse hydrogen into helium. Stars that accrete mass greater than 0.8 $M_\odot$ follow the 'main sequence'. The main sequence is a path on the Hertzsprung-Russell (HR) diagram, which shows the relationship between the luminosity and the temperature of a star, and provides a schematic for the evolutionary paths of stars (Figure 1.1a). Different regions in the HR diagram represent different times in a star's life and all of

the stars in each section have the same characteristics and parameters; however, each star moves through each region depending on its mass. The main sequence process begins when stars stabilise their thermonuclear hydrogen-helium fusion. It contains 90% of all stars, which are in hydrostatic equilibrium. There are two major divisions, the low- and intermediate-mass stars ($1-8$ $M_\odot$) and massive stars (8+ $M_\odot$, maximum observed is approximately $120-200$ $M_\odot$ [Oey and Clarke, 2005]).
Unlike the low-medium mass stars which have lifetimes of a few trillion years, massive stars have short lifetimes of only a few million years. When massive stars run out of hydrogen they inflate into giants and leave the main sequence. Stars with a mass greater than $10\,M_\odot$ will continue to fuse heavier elements until they have an iron core. At this stage, the core will collapse and the star becomes a Type 2 supernova. Stars between $8-10\,M_\odot$ are not massive enough to heavy elements, which means they will lose their outer shell and become white dwarfs. The low- and intermediate-mass main sequence stars - when out of hydrogen - will become red giants. Figure 1.1b shows the evolutionary track specifically for a typical main sequence star, with the same mass as the sun. Once a star is a red giant, the thermonuclear fusion of hydrogen in its shell starts. There are three different types of red giants:

- Red Giant Branch - these fuse hydrogen into helium in their shell and have a helium core. These are the most common red giants.
- Red Clump - are cooler and are fusing helium to carbon in their cores.
- Asymptotic Giant Branch (AGB) - these stars have a helium shell and have a core that is burning oxygen into carbon.

Red giants are very luminous, even though they have a low-energy envelope. The luminosity is a result of its size which is tens of hundreds of times the radius of our Sun. This brightness makes them a popular target in astronomy. Red giants have an average temperature between approximately $4000-5000\,K$.

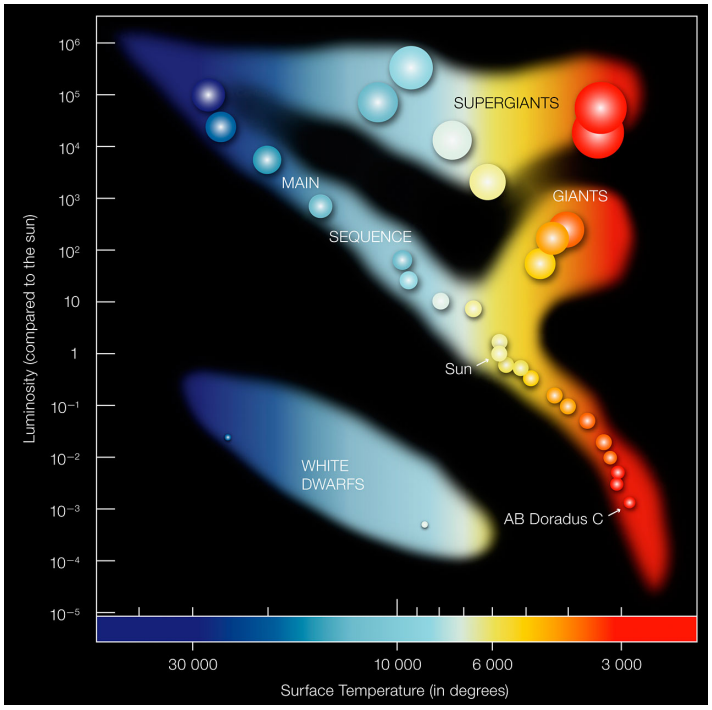

(a)

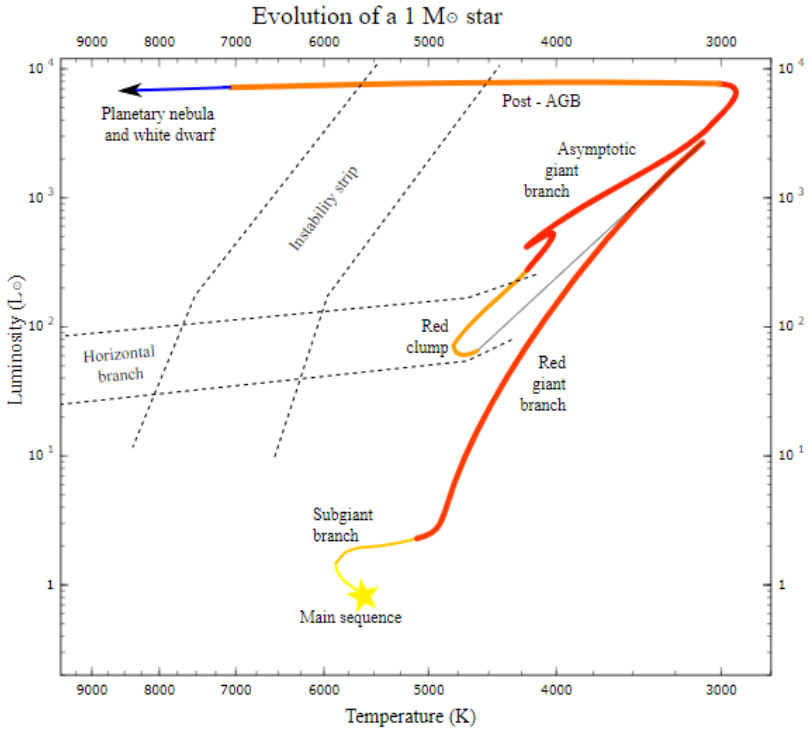

(b)

Figure 1.1: (a)Hertzsprung-Russell diagram displaying the main sequence (diagonal band that goes from bottom right up to the top left), the hot luminous stars (top left) along with the cooler dim stars (bottom right corner). (b) The evolutionary track (red line) of a typical main sequence star ($1M_{\odot}$).

1.1.4 Star Clusters

Globular clusters

Globular clusters are very dense and contain up to a million stars. They are very bright even at great distances and are mostly found in the halo of the Galaxy. They are a good example of a simple stellar population as they contain such a large range of stars which are at essentially the same distance, possibly the same age, and same chemical composition. Over the last few decades, globular clusters have been heavily studied and shown to have more complexity than first thought. They have strange variations of chemical compositions between stars and the clusters evolve dynamically [Gratton et al., 2004]. As well as this, they contain a strange array of stars such as millisecond pulsars, blue stragglers, O- and B-subdwarfs and cataclysmic variables. A comprehensive model of formation and evolution for such globular clusters is yet to be found. Some clusters hold stars which have the same stellar evolution implying the stars have formed at the same time. Others have varying populations; for example, a globular cluster in the Large Magellanic Cloud has bimodal age distribution, which suggests that at some point these clusters may have encountered another GMC which started a second round of star formation [Piotto, 2008]. The other theory for bimodal population is that two formed clusters collided and merged to form a cluster with a wide age range [Amaro-Seoane et al., 2013]. There are more than 150 known globular clusters in our Galaxy; however other galaxies, particularly elliptical galaxies, have been observed to have thousands of clusters.

Open clusters and spin alignments

Observations show that open clusters are forming in the present epoch of our galaxy. In theory, it is possible to examine the formation of these clusters; however, the opaque nature of GMCs means that the early stages cannot be fully investigated. Recent literature suggests that 70 to 90% of stars form in clusters [Lada and Lada, 2003]. Recent advances in technology with space-based telescopes have made it possible for clusters to be observed with high accuracy, not only in our galaxy but in other galaxies as well. Observations of clusters in other galaxies show their overall spatial distributions

and give the "big picture". However, observing within our own galaxy gives us a more accurate set of properties of each star as well as the cluster as a whole [Kharchenko et al., 2012]. The disadvantage in observing local open clusters is the extinction between us and the clusters which limits us to observe a few kiloparsecs around the Sun [Kharchenko et al., 2013].

Open clusters are less dense in comparison to globular clusters; they generally contain only a few hundred stars. Young open clusters are contained within molecular clouds which are ionised by the radiation. Stars that form from one GMC are gravitationally bound systems that have the similar parameters, such as chemical composition, age, velocity, extinction, proper motions and metallicity. This association means they are dynamically linked and can be used to study not only formation but also evolution of stars in clusters. Recent star formation models show that the angular momentum of the molecular cloud, which is dependent on the small-scale turbulence and magnetic field disruptions, is conserved even after star formation. The spin alignment of the stars in the formed cluster is directly dependent on the amount of kinetic energy of the progenitor cloud, and the proportion of rotational versus turbulent pressure support [Corsaro et al., 2017].

1.2 Asteroseismology

Asteroseismology is the study of stellar oscillations, which can be used to probe the interior of stars. The oscillations are directly related to the internal properties of the stars [Aerts et al., 2010]. Different oscillation modes of a star penetrate to different depths of the star which enables each layer to be studied using the frequency differences of the modes. Asteroseismology aims to improve the understanding of the internal structure of stars, which in turn will improve our understanding of star formation and evolution [Aerts et al., 2010].

The most basic type of oscillation is radial, where spherical symmetry is conserved. Mathematically, the radial displacement can be described using Sturm-Liouville theory

[Chaplin and Miglio, 2013]. The differential equation can be used to obtain the eigenvalues which correspond to the eigenfrequencies. The fundamental radial oscillation mode identified by the smallest frequency is inversely proportional to the oscillation period. Red giants, Cepheids and RR Lyrae stars all oscillate radially. The number of nodes of the eigenfunction between the centre and the surface of the star is represented by the radial wave number n. If there is additional transverse motion, this is known as a non-radial oscillation. Non-radial oscillations have further wavenumber l and m, which refer to the degree and azimuthal number of spherical harmonic $Y_l^m(\theta, \varphi)$ respectively. l is the number of nodal lines on the stellar surface and m is the number nodal lines that pass through the rotational axis. Figure 1.2 shows a Doppler map of the radial velocities of the structure of a non-radial oscillator, where the blue regions are moving outward (blueshift) and the red regions are moving inwards (redshift). For one oscillation cycle that is completed, each region is blueshifted and redshifted once [Aerts et al., 2010].

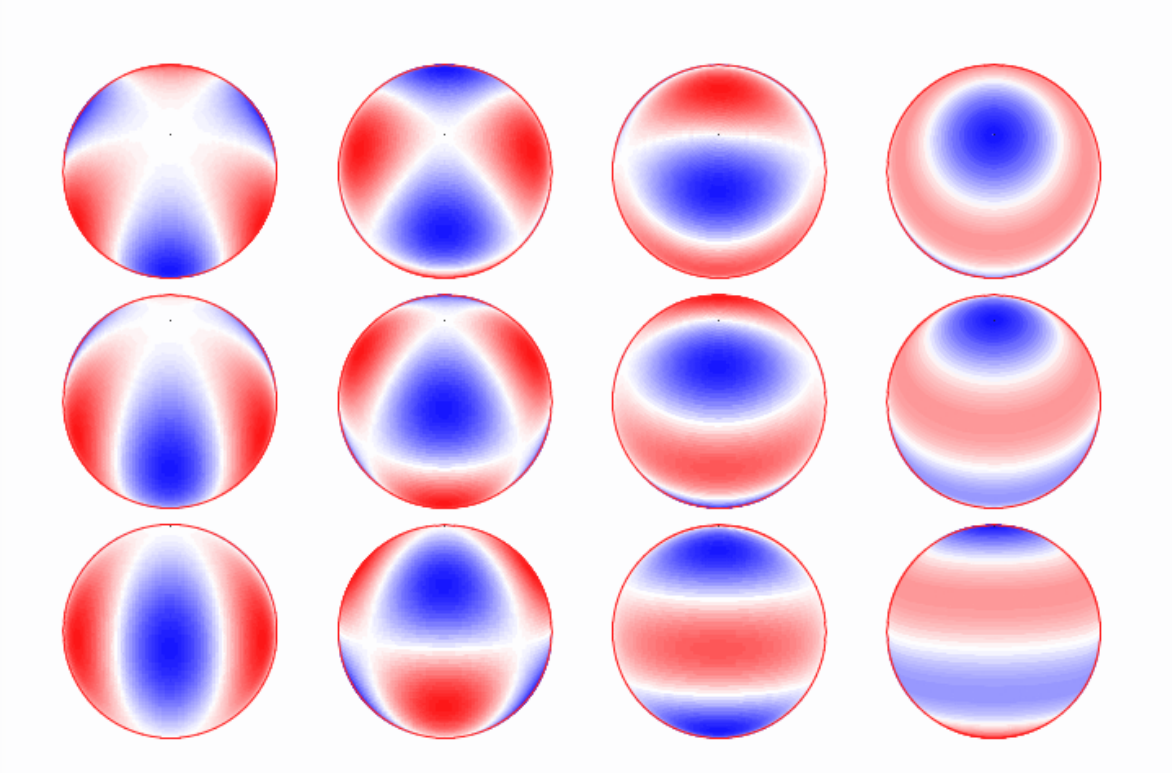

Figure 1.2: Doppler maps of radial velocities on a non-radial oscillator. The each row shows the inclination angle for $i = 30°$, $i = 60°$, $i = 90°$ respectively. l is equal to 3 for all the examples; m goes from 0 (right most column) to 3 (left most column). White lines are nodal lines. Image: Aerts et al. [2010]

There are four types of excitation mechanisms which drive the stellar oscillations; ϵ mechanism, $k - \gamma$ mechanism, convective and stochastically excited [Handler, 2013]. ϵ mechanism oscillations are a result of variations in the nuclear reaction rate. Compression of the nuclear burning region increases the temperature which in turn produces more energy. The excess energy results in an expansion, and a decrease in pressure and energy generation [Handler, 2013]. This variability of energy production produces the oscillations. These types of oscillations have been proposed but are yet to be observed [Rosseland and Randers, 1938].

In the $k - \gamma$ mechanism, as the opacity increases with temperature, the energy from inside the star is temporarily stored in layers which are either fully or partially ionised [Handler, 2013]. The extra energy is released when the layers return to their equilib-

rium state. For the whole star to oscillate, the layers must be in a specific position and hence the oscillations are directly dependent on the properties of the star such as temperature, luminosity and chemical composition [Aerts et al., 2010]. This mechanism is also known as the Eddington Valve as the layers act like a valve; this can be used to explain the variability of most pulsating stars [Handler, 2013].

Another valve-like mechanism is known as convective blocking (or convective driving). In this mechanism, the oscillation is a result of the convection zone blocking the energy from the interior of the star. The energy released during compression and expansion of the convection zone drives the periodic oscillation [Handler, 2013]. White dwarfs and γ Doradus stars are believed to be at least partially excited by this mechanism. Both the $k - \gamma$ and convective blocking mechanisms are self-excited and are known as free oscillations [Aerts et al., 2010]. In these cases, a forced oscillation would be one that is induced from tidal forces by a binary companion.

The oscillations of the Sun or a star similar to the Sun (solar-like) are not self-driven but are a product of the turbulence in the stellar convection zones. These are said to be stochastically driven and are intrinsically stable [Brown and Gilliland, 1994]. The convective motions of the outer layers generates acoustic noise which results in oscillations [Aerts et al., 2010].

The two restoring forces required for stellar oscillations are both standing waves that are driven by pressure and gravity. The gravity force, is the buoyancy force and the modes are known as the g-modes. G-modes are most prominent in non-radial oscillations. The other standing waves, the pressure driven modes, are known as p-modes [Aerts et al., 2010].

1.2.1 Solar-like oscillations

For a star to be oscillating in a solar-like manner, it needs to have near-surface convection [Chaplin and Miglio, 2013]. These oscillations have multiple modes excited to observable amplitudes. As this results in geometric cancellation, only $l < 4$ modes can

be observed in these types of stars [Christensen-Dalsgaard, 2018]. P-modes for solar-like oscillations have relatively high frequencies, short periods and are standing sound waves. The asymptotic nature of p-modes allows us to characterise their properties, which means the cyclic frequency can be found using Equation 1.2.1.

$$\nu_{nl} \simeq \Delta\nu \left(n + \frac{l}{2} + \epsilon \right) \tag{1.2.1}$$

In this equation, ϵ is the phase, which is frequency-dependent and is also directly related to the star's near-surface properties. $\Delta\nu$ is the large frequency separation and is defined as in Equation 1.2.2 [Christensen-Dalsgaard, 2018].

$$\Delta\nu = \left(2 \int_0^r \frac{dr}{c} \right)^{-1} \tag{1.2.2}$$

where c is the adiabatic speed of sound and the integral is over the radius r, which is the distance from the centre and is constrained between the centre of the star and the surface radius of the star R [Christensen-Dalsgaard, 2018]. These definitions can be used to show the relationship between the large separation frequency, $\Delta\nu$, and the stellar mean densities to be as presented in Equation 1.2.3.

$$\Delta\nu \propto \left(\frac{M}{R^3} \right)^{\frac{1}{2}} \tag{1.2.3}$$

where M is the mass of the star. Furthermore, using the definitions from Equations 1.2.1 and 1.2.2, the small frequency separation can be found using Equation 1.2.4.

$$\delta\nu_{nl} = \nu_{nl} - \nu_{n-1,l+2} \simeq -(4l+6) \frac{\Delta\nu}{4\pi^2 \nu_{nl}} \int_0^R \frac{dc}{dr} \frac{dr}{r} \tag{1.2.4}$$

The second expression in 1.2.4 is only valid for main sequence stars. $\delta\nu_{nl}$ is dependent on the chemical composition of the star, as for an ideal gas $c^2 \propto T/\mu$, where μ is the mean molecular weight and T is the temperature. This relation can be used to determine the hydrogen to helium ratio and hence the age of the star [Christensen-Dalsgaard, 2018]. Figure 1.3 shows an example power spectrum (Fourier transform of a light curve) of two red giants as observed by *Kepler*: KIC 6779699 (hydrogen-shell burning on the red giant branch) and KIC 4902641 (helium burning in its core).

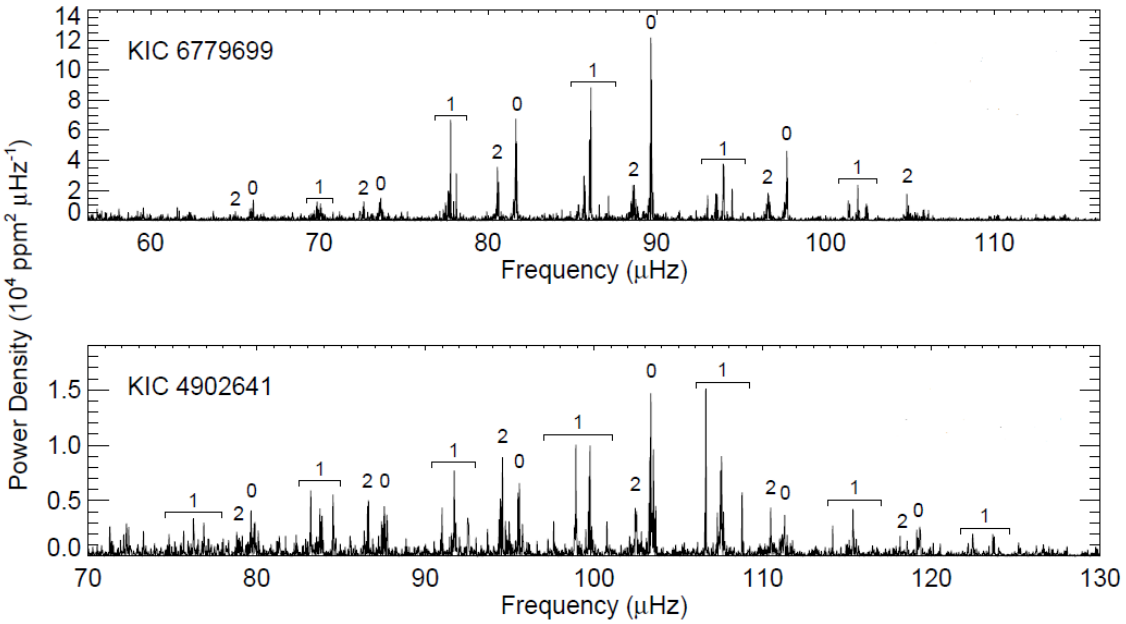

Figure 1.3: Power spectra of two red giants as observed by *Kepler*, with the modes $l = 0$ $l = 1$ and $l = 2$ identified in the figure. Top: KIC 6779699, which is a hydrogen-shell burning red giant with $\nu_{max} = 87$ μHz and $\Delta\nu$ of 8 μHz. Bottom: KIC 4902641 which is burning helium in its core has ν_{max} of 100 μHz and $\Delta\nu$ of 7.89 μHz [Bedding et al., 2011]. Image: Bedding et al. [2011]

G-modes act through buoyancy on density and are characterised by the buoyancy or the Brunt-Väisälä frequency, N and is defined by Equation 1.2.5 [Aerts et al., 2010].

$$N^2 = g\left(\frac{1}{\Gamma_1}\frac{d\,ln\,p}{dr} - \frac{d\,ln\,\rho}{dr}\right) \tag{1.2.5}$$

where p is the pressure, ρ is the density, g is the local gravitational acceleration and Γ_1 is the adiabatic compression. The detection of g-modes in solar-like oscillations has been debated as N^2 is negative in the convection zones and hence the gravity waves dissipate fairly quickly. In more evolved stars, the gravitational acceleration and N^2 is high as they have a more compact core. This means the g-modes have very high frequencies, similar to those detected for p-modes; this results in the mixed-modes phenomenon [Christensen-Dalsgaard, 2018].

Stochastically-excited modes assume that the average amplitude is independent of m,

for any l and n. Observations show that the amplitude is dependent on the inclination angle of the rotational axis with respect to the line of sight [Gizon and Solanki, 2003]. Stars which have spherical symmetry also have frequencies that are independent of m. However, this changes if a star loses its spherical symmetry and as a result rotation is affected. Rotation produces a splitting which can be defined as Equation 1.2.6 [Christensen-Dalsgaard, 2018].

$$\nu_{nlm} = \nu_{nl0} + m\delta_{rot}\nu_{nlm} \tag{1.2.6}$$

The average rate of rotation is denoted by δ_{rot}.

Scaling relations

The study of helioseismology can be used to estimate the parameters of solar-like oscillators other than the Sun. Using $\Delta\nu$, ν_{max} and T_{eff}, mass (M) and radius (R) of the solar-like star can be derived. This method compares $\Delta\nu$ and ν_{max} of the star with those of the Sun and estimates mass and radius through scaling. The relationship shown in Equation 1.2.7 was derived by Kippenhahn et al. [1990] for any two stars that are homologous with radii R and R', and mass M and M'.

$$\frac{\Delta\nu'}{\Delta\nu} = \left(\int_0^R \frac{dr'}{c}\right)\left(\int_0^{R'} \frac{dr}{c'}\right)^{-1} = \left(\frac{M'}{M}\right)^{\frac{1}{2}}\left(\frac{R'}{R}\right)^{-\frac{3}{2}} \tag{1.2.7}$$

This was then applied to the Sun which gives Equation 1.2.8

$$\Delta\nu \approx \Delta\nu_{\odot}\left(\frac{M}{M_{\odot}}\right)^{\frac{1}{2}}\left(\frac{R}{R_{\odot}}\right)^{-\frac{3}{2}} \tag{1.2.8}$$

Red Giants

Red giants show a complicated mixed-mode frequency structure that is directly linked to the interior of the star. Observations of rotational splitting confirm the cores of red giants spin faster than the surface by a factor of 10 [Beck et al., 2012]. This high rotation is expected in a red giant, as the evolution of the star onto the red giant branch involves a strong contraction of the core [Christensen-Dalsgaard, 2018]. The observations also suggest that there must be an angular momentum transfer mechanism present

in these stars as the theoretical rate of rotation for a red giant core is expected to be much higher. It is not currently understood what this mechanism could be, although internal gravity waves are believed to play a part in this [Christensen-Dalsgaard, 2018].

Compared to other solar-like oscillators, red giants pulsate with larger amplitudes and longer periods. This means they can be observed easily but need to be observed over a long and continuous period. Initially, ground-based studies attempted to observe red giants. However, they were hampered by the long observing periods required to resolve low frequencies [Christensen-Dalsgaard, 2018]. The new technology of CoRoT and *Kepler* (see Section 1.4.1) enabled precise measurements of light curves of stars pulsating with non-radial and radial modes. *Kepler* observations made it possible to measure low frequencies with long periods [Christensen-Dalsgaard, 2018]. In an early analysis of CoRoT data, De Ridder et al. [2009] showed that red giants show a full range of solar-like oscillations. This was an important advancement, and with *Kepler* data's mixed mode identification capabilities it became possible to obtain a full diagnostic of red giant oscillations [Beck et al., 2011].

1.3 Inclination angles

Inclination angles of stars' spin axis relative to our line of sight provide important information. In extra-solar systems the inclination angle (i) can be used to determine the mass of orbiting planets. Using spectroscopic measurements we can obtain $v \sin i$ where v is the rotational velocity of the star at the equator [Gizon and Solanki, 2003]. This coupled with the angular velocity (Ω) - an asteroseismic parameter - and i, the radius of the star can also be estimated. Recent studies show that the alignment of i in stars in open clusters are not isotropically distributed [Corsaro et al., 2017]. Both single and binary members of a star cluster show this preference in inclination angles, which is suggested to be the result of the angular momentum being transferred from the GMC to the stars [Corsaro et al., 2017]. For this alignment to change, strong tidal interactions between binaries must be present [Gizon and Solanki, 2003]. However publications such as Kamiaka et al. [2018] and Kamann et al. [2018] issue caution in interpreting

results from C2017 as the outcomes may be affected by potential systematics of *Kepler*.

The standard method in obtaining i, until 2003, was using the periodic Doppler shifts in a star's spectrum to find transiting planets. This technique would return $M_p \sin i_p$, where M_p is the mass of the planet and i_p is the orthogonal vector to the planets' orbital plane relative to the line of sight. i_p can be approximated to i as they are both expected to be similar [Gizon and Solanki, 2003]. Gizon and Solanki [2003] introduced a new technique to extract the inclination angle of Sun-like stars. The ratio of dipole components of $m = \pm 1$ and $m = 0$ are strong functions of i, Gizon and Solanki [2003] uses this dependency to extract the inclination angle. A similar method which used solar dipole modes of oscillations, obtained the inclination of the Sun within 5° of the actual value [Gizon and Solanki, 2003]. They also showed that using their method, the inclination angles of stars could be accurately retrieved given that $i \gtrsim 30°$ and the star had rotational velocity twice as much as the Sun.

C2017 use the same dipole mode oscillation technique to analyse 48 red giants in two open clusters - NGC 6791 and NGC 6819. Both clusters are more than one gigayear old. C2017 identify 380 rotationally split dipolar mixed modes - out of 3900 oscillation modes - for the red giants [Corsaro et al., 2017]. They find that 70% of stars show strong alignment (defined by an alignment coefficient $\alpha > 0.7$). They also calculate the probability of this alignment being random to be; 1 in 10^9 for NGC 6791 and 1 in 10^7 for NGC 6819. These findings, and N-body simulations performed by C2017, conclude that angular momentum is inherited by the stars from the clouds from which they formed.

Kamman et al (2018) use line of sight (LOS) velocities - not obtained using astero-seismology - to analyse cluster dynamics and obtain stellar inclinations for the same clusters as C2017 (NGC 6791 and NGC 6819). They find similar results for NGC 6791 ($i = 45°$) but with high uncertainties and classify it as a promising target for future research. However, NGC 6819 showed no significant rotation using their analysis and hence they do not extract the inclination angles for this cluster. The studies discussed

above confirm that asteroseismology is an effective tool in studying star formation and offers a unique perspective into the internal structure and properties (such as rotation, inclination, mass and chemical composition) of stars.

1.4 Data and telescopes

This section discusses the choices for data and discuss the technical specifications of the telescopes.

1.4.1 Kepler and the K2 Mission

Kepler was launched in March 2009 in an Earth-trailing orbit and was designed to hunt for exoplanets using the transit technique [Barentsen, 2019]. In its primary mission *Kepler* observed over 150,000 stars, with a continuous sampling of either 30 minutes (long cadence) or 1 minute (short cadence). The original mission was planned to last three years and then was later extended for another three years, of which the telescope completed one. In July 2012, one of the four reaction wheels - which aided the telescope with fine pointing - stopped turning. NASA attempted to fix this as the extended mission would not be possible without all four wheels. However, in July 2013 another reaction wheel stopped turning and NASA announced they were no longer attempting to fix this. In May 2014, NASA approved a new mission for *Kepler*: Second Light (K2). K2 was planned to collect data for not only exoplanets but also star formation, supernova explosions and solar system objects [Wall, 2013]. The new mission had a much lower pointing precision and hence had increased noise to 300 parts per million, from *Kepler*'s 20 parts per million. K2 made use of the solar photon pressure to balance and stabilise the spacecraft; a conceptual schematic is shown in Figure 1.4. The spacecraft is rotated approximately every 80 days in the K2 mission, whereas it was rolled every 93 days for *Kepler*, to avoid sunlight from entering the telescope. In October 2018, NASA announced that the spacecraft has officially retired as it was out of fuel.

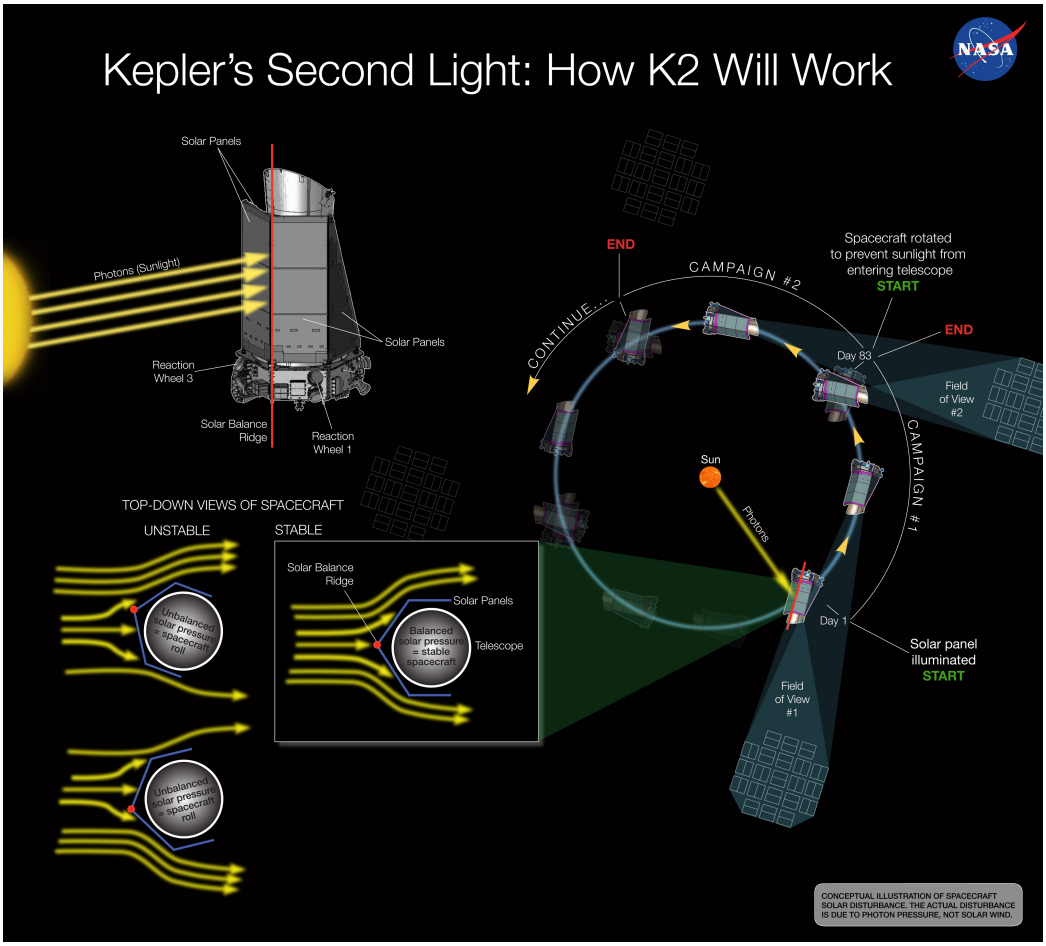

Figure 1.4: A conceptual illustration of how the spacecraft was stabilised using photon pressure from the Sun in the new K2 mission. The observing period was approximately 80 days after which a new campaign started. Image: NASA Ames/W Stenzel [Johnson, 2017]

The spacecraft has a 0.95 m Schmidt telescope, which consists 21 of CCD modules. Each module has 4 output channels but 3 modules were lost as of July 2018, hence K2 only has 18 active modules [Barentsen et al., 2019]. The photometer has one broad bandpass of range 420 - 900 nm [Barentsen et al., 2019]. K2 has a Nyquist frequency of 287 μHz this means that the highest observable frequency is 270 μHz and the lowest observable frequency of approximately 10 μHz [Stello et al., 2015]. We use data from *Kepler* space telescope for asteroseismological analysis, as its second mission has new scientific goals. One of these goals is to use the 360° ecliptic field of view to study oscillations in red giants.

1.4.2 Gaia

Gaia was launched on the 19^{th} of December 2013 with an expected mission life of 5 years. The mission has since been extended for another 3 years. The main aim of Gaia was to investigate dynamics, structure, kinematics and hence the evolution of our galaxy [Agency, 2019]. The spacecraft consists of the payload module, the mechanical service module, and the electric service module. The mechanical service module consists of: a flat sunshield which protects the spacecraft, and more importantly the payload module from sun light, the thermal control system; and the thrusters of the propulsion system. The electric module holds the communication subsystems, central computer, data handling subsystems and the power subsystem [European Space Association, 2013]. The payload has been built around the optical bench and contains 3 main instruments:

1. The astrometric instrument (ASTRO). This provides five astrometric parameters and is dedicated to stellar angular measurements. The parameters measured are:
   (a) Two angles of stellar position.
   (b) Two time derivatives of position for the proper motion.
   (c) Parallax.
2. The photometric instrument. This is the chromaticity calibrator for ASTRO and provides constant stellar spectra for astrophysics between 320 and 1000 nm.
3. The Radial Velocity Spectrometer (RVS). This provides radial velocities and high resolution spectra for 847 to 874 nm.

The payload contains two identical telescopes which have a separation angle of 106.5°. Figure 1.5 illustrates the schematic of the payload module.

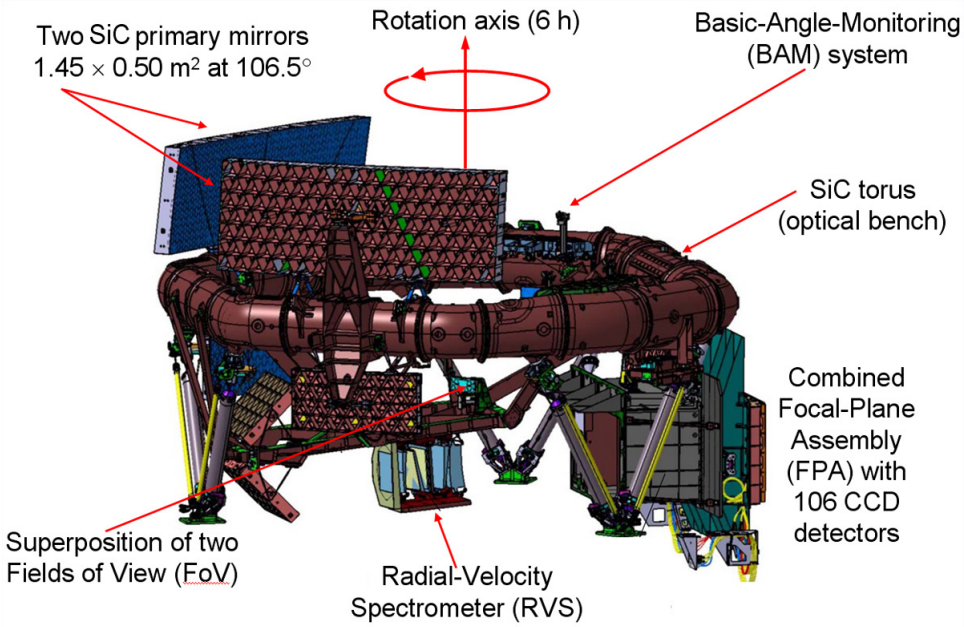

Figure 1.5: Gaia Payload. Image: ESA [European Space Association, 2013]

One of Gaia's scientific goals is to improve our understanding of stellar structure and evolution. With plans to observe 1 billion stars in the Galaxy, Gaia measures the position and motion of stars 200 times more accurately than its predecessor, Hipparcos [Agency, 2019]. The high-precision data from Gaia is be utilised in this study to analyse the proper motions of stars in open clusters.

Chapter 2

Clusters

2.1 Cluster selection

Red giants (RGs) are low- to intermediate - mass stars which have evolved off the main sequence. They are very luminous and as a result their solar-like oscillations can be relatively easily detected. Hence they are ideal targets for asteroseismological analysis. When selecting target clusters for analysis, it was therefore important that the open clusters were at least one gigayear (Gyr) old, as the aim of the study is to show that the angular momentum retains its signature after that time, and are RG rich. The RG population was a major factor in selecting clusters as the higher the number of RGs, the greater the accuracy of the results in this study. The target selection process began by listing all known clusters using the galactic open cluster catalogue of Kharchenko et al. [2013] (hereafter K2013). The Kharchenko catalogue of open clusters was originally published in 2004 with 109 clusters [Kharchenko et al., 2005a]. Later updates were added: 520 clusters in 2005 [Kharchenko et al., 2005b]; 642 in 2012 [Kharchenko et al., 2012] (hereafter K2012); and finally 3006 clusters in 2013 [Kharchenko et al., 2013]. The latest update to the method for determining cluster membership was made in K2012 in which the kinematic probability equation was updated to include errors (discussed further in Section 2.2.1). In K2012, the authors assign each star in the field a kinematic and photometric probability, and then the combined probability is used to determine whether a star is a member of a certain cluster.

2.1. Cluster selection

In this study, the K2013 catalogue was cross-matched with the K2 catalogue to ensure that K2 data was available for the asteroseismological analysis. The potential cluster target list included fifty-one clusters, of which five were older than one Gyr. Table 2.1 lists the five potential open clusters and shows the parameters for each cluster from the K2013 catalogue and Table 2.2 shows the stellar mass estimates and apparent sizes of the final selected clusters. An estimate for stellar mass for Ruprecht 131 and Ruprecht 139 is not included as there are currently no reliable sources which estimate these. Ruprecht 131 and Ruprecht 139 are little studied clusters with a small number of cluster members, which implies a small RG population. Hence, these clusters were removed as potential targets. The memberships and the methods of calculating membership for each cluster varies through different papers. This work uses the parameters of the latest publications for initial values to further calculate the probabilities which determine the membership. The most used publications are K2012, K2013, Stello et al. [2016] for M67, Curtis et al. [2013] for Ruprecht 147 and Christian et al. [1985] for NGC 2158.

Table 2.1: Parameters from K2013 [Kharchenko et al., 2013] for the short-listed potential cluster targets. (*) were not included as final selected target clusters.

Cluster name	Log (age)	Distance (pc)	RA (°)	Dec (°)	Members
Ruperecht 131*	9.17	600	267.31	-29.25	30
Ruprecht 139*	9.05	550	270.25	-23.53	7
Ruprecht 147	9.39	175	289.17	-16.3	49
NGC 2158	9.33	4000	91.857	+24.092	346
NGC 2682 (M67)	9.41	908	132.85	11.8	637

Table 2.2: Apparent sizes (literature values) and stellar mass estimations of final cluster targets. The mass estimate for M67 is from Hurley et al. [2005] and the mass estimate for R147 is from Yeh et al. [2019]

Cluster name	Apparent size	Stellar Mass
M67	27'	2000
R147	1° 15'	234 ± 52
NGC 2158	8.4'	-

2.2 Cluster Membership

Cluster membership is fairly elusive, and it is a challenge to determine how massive a cluster is. This is because some stars shine differently in each photometric colour and hence not all can be detected by one telescope. There have been many attempts to normalise and find a reliable method for cluster membership. Most methods use the properties listed below to determine membership, as the stars that form from the same molecular cloud will have similar properties:

- Proper motions: Proper motions are the apparent motions of a star on the celestial sphere when measured orthogonally to the line of sight and are measured in milliarcseconds per year (mas/yr). This is also known as the angular velocity of the star across the sky. All motion towards or away from the Sun is ignored in this measurement [Majewskki, 2018]. As the clusters are loosely gravitationally bound, the stars within them move across the celestial sphere at the same rate.

- Radial Velocities: These are the velocities of the stars relative to the Sun; it is also known as the line-of-sight velocity and is measured in kilometres per second (km/s). The stars would have comparable radial velocities as the cluster due to the gravitational binding.

- Photometry: The stars in a cluster are generally close to each other and hence they will generally all have similar extinction.

When calculating cluster memberships, we need to consider not only the dynamical properties such as proper motions and radial velocities, but also photometric properties and distances of the stars. This work uses proper motion probabilities in combination with distance probabilities to determine the membership for each cluster. Methods from K2012 were used for the kinematic probabilities using proper motions from Gaia Data Release 2 [Brown et al., 2018]. The Gaia parallax was used to obtain the distance for each star, then the known distance was used to assign a distance probability. The sections below discuss the methods and results from this analysis.

2.2.1 Gaia data, astrometry and errors

Gaia data was downloaded from the online catalogue ViZieR [Ochsenbein et al., 2000] for all columns listed in Table 2.3 in the form of `.tsv` files. The data has an along scan measurement which consists of the precise time at which the image centroid passes a fiducial line on the CCD [Lindegren et al., 2018]. Gaia measures three magnitudes; apparent G magnitude, BP (BP_mag in Table 2.3) with a wavelength range of 330-680 nm and RP (RP_mag in Table 2.3) with a wavelength range of 630 - 1050 nm. Gaia archives calculate an absolute G magnitude value using Equation 2.2.5. The apparent G magnitude is referred in this study as G_{mag} and absolute G is referred to as G. For each of the three selected clusters in Table 2.1, the literature values of apparent size were multiplied by 1.5 and the data for each cluster was downloaded for the box size. For M67, this box size was 40.5' square, for R147 the box size was 1.875 degrees square and for NGC 2158 the box size was 12.6' square centred on the cluster centre.

Table 2.3: The columns of Gaia data downloaded of the three selected clusters.

Column	Description
RA_ICRS	Barycentric right ascension
DE_ICRS	Barycentric declination
Plx	Absolute stellar parallax
e_Plx	Standard error of parallax
pmRA	Proper motion in right ascension
e_pmRA	Standard error of proper motion in right ascension
pmDE	Proper motion in declination
e_pmDE	Standard error of proper motion in declination
NgAL	Number of good observations along scan (AL)
chi2AL	AL chi-squared value
Gmag	G-band mean magnitude
e_Gmag	Standard error of G-band mean magnitude
BPmag	Integrated BP mean magnitude
e_BPmag	Standard error of BP mean magnitude
RPmag	Integrated RP mean magnitude
e_RPmag	Standard error of RP mean magnitude

During the data processing the Gaia team found a disparity in the formal errors, which needed to be corrected. Instead of re-computing the entire astrometric solution, a re-weighting of the errors was calculated. The alternative solution - also provided by the Gaia team in a publication - was applied to this data set [Lindegren et al., 2018]. This statistical correction was calculated by quadratically adding the excess noise ϵ to the formal uncertainties σ_η [Lindegren et al., 2018]. The archive provides a χ^2 value which is defined as

$$\chi^2 = \sum_l \frac{R_l^2}{\sigma_{\eta,l}^2 + \epsilon_a(t_l)^2} \tag{2.2.1}$$

where R is the residual of along-scan observation l, and ϵ_a is excess attitude noise, which is a function of time but is the same for all sources at any given time. When

calculating χ^2, excess source noise (ϵ_i) is not included in the denominator as it would mean χ^2 is always greater than the degrees of freedom (ν). χ^2 is a computation of how well a source fits a single-star model. This can then be used to calculate the unit weight error, u, which is a "goodness-of-fit" defined as

$$u = \sqrt{(\chi^2 + \nu)} \tag{2.2.2}$$

The unit error, u, was computed according using Equation 2.2.3.

$$u = \sqrt{\frac{\texttt{chi2AL}}{\texttt{NgAL}} - 5} \tag{2.2.3}$$

This correction was then applied to the data. The model created by the Gaia team suggested that u should always have a mean of 1. However this was not the case for sources brighter than Gaia G magnitude $\simeq$ 17. The mean for brighter sources was much higher at $u \approx$ 1.2 - 1.4. This was the result of a bug in the source update algorithm and it was named the 'DOF' bug. The actual astrometric parameters were not significantly affected but formal uncertainties needed to be corrected. As the data set used in this study only contains RGs which are bright stars, it was important to apply this correction. The Gaia team refers to this acceptable quality data as "good". This "goodness" was determined by using conditions given by

$$u < 1.2 \times max(1, e^{-0.2(G-19.5)}) \tag{2.2.4}$$

and

$$G = Gmag + 5\log\left(\frac{\varpi}{100\,\text{mas}}\right) \tag{2.2.5}$$

where $Gmag$ is the observed value from the Gaia archives, and ϖ is the parallax and hence $\frac{\varpi}{100\,\text{mas}}$ is the parallax divided by 100 milliarcseconds. Figure 2.1 shows the data for each of the three selected clusters, with the red line showing the cut-off for the "bad" data. All the data points lying below the red line were accepted as being "good" data points with reasonable errors.

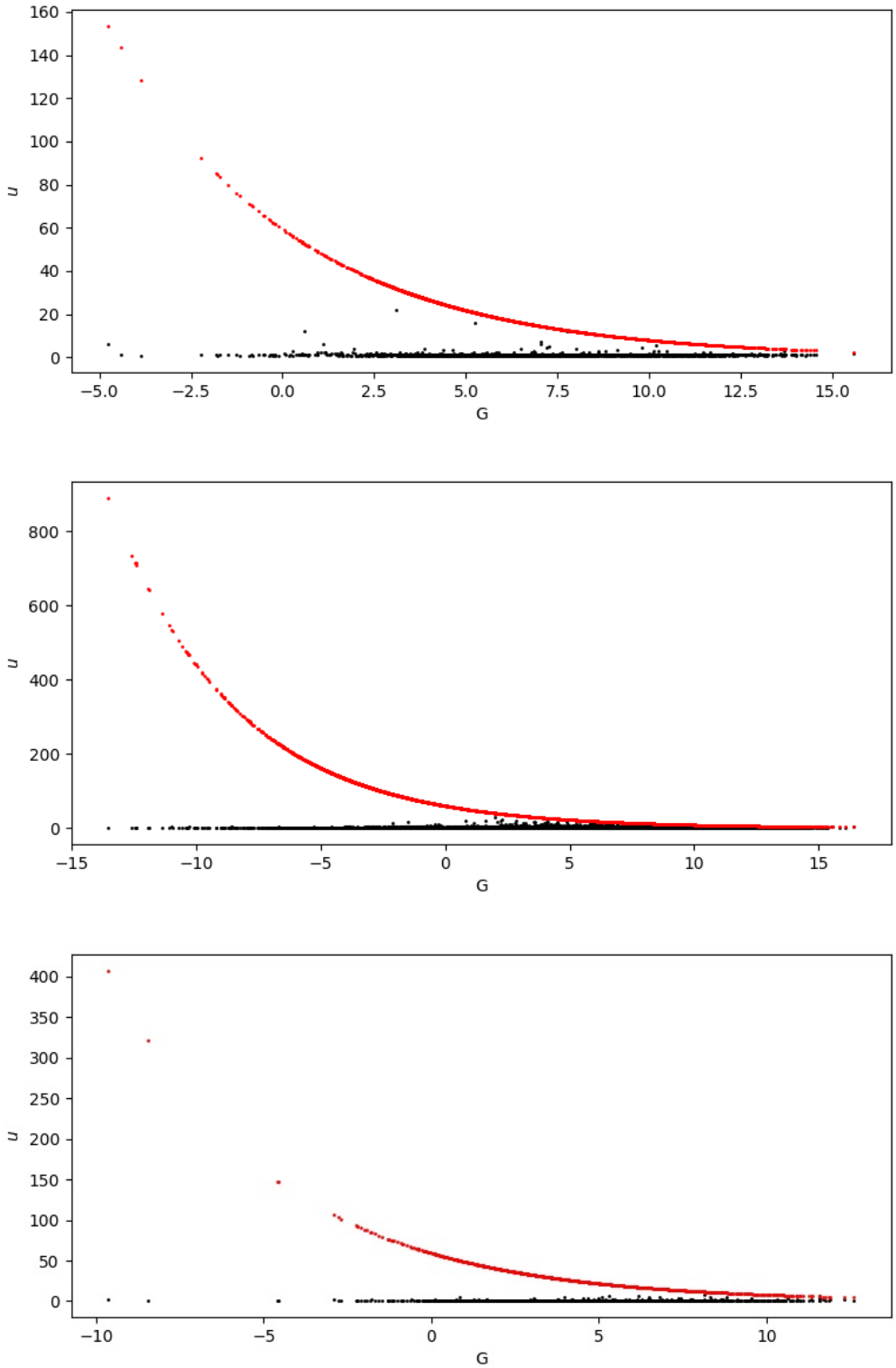

Figure 2.1: The unit weight error (black dots) plotted vs absolute G magnitudes for (top) M67, (middle) R147, and (bottom) NGC 2158. The red dots are the plot of Equation 2.2.4 for unit weight error u. Acceptable values of u lie below the red line for a given G magnitude.

Calculation of membership probabilities

Initially an attempt was made to select cluster members using an iterative method of sigma clipping. This method took the mean of the proper motions in both right ascension (RA) and declination (DEC) and used it to remove all stars that were not within two standard deviations. Figure 2.2 shows the DEC proper motion vs RA proper motion for an example cluster (M67). The cluster proper motion is fairly obvious. However, a problem with this method is that the mean proper motions of all the stars in the field may not necessarily be the mean proper motion of the cluster. This is especially the case for clusters with a large apparent size, such as R147 which has an apparent size of 1.25°, and for which there may be a large number of contaminating foreground or background objects that are not cluster members. Following the application of the sigma clipping technique, the membership was still somewhat uncertain due to the fact that distance was not accounted for.

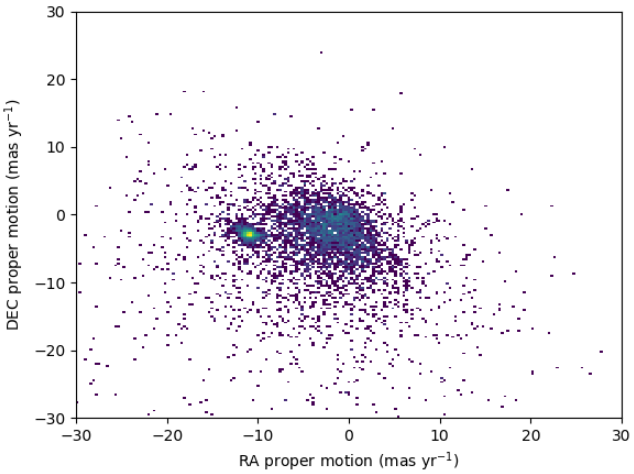

(a)

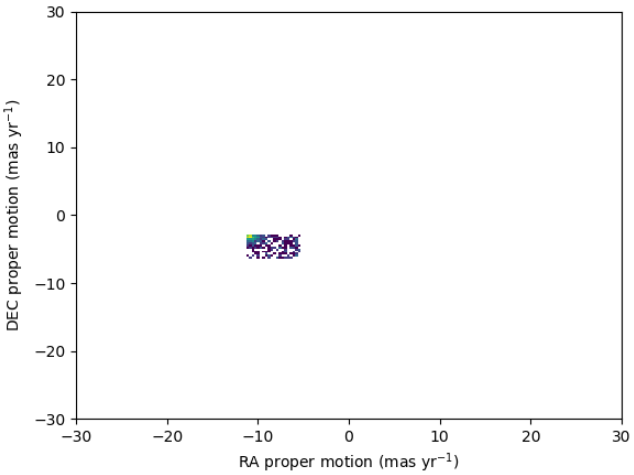

(b)

Figure 2.2: The proper motion for M67 in DEC vs RA for (a) a field of 35' and (b) the selected sigma-clipped data

Kinematic Probabilities

As mentioned in Section 1.1.4, the stars in open clusters form together and hence have the similar dynamics. These dynamics, that is their proper motions and radial velocities, can therefore be used to determine membership. Following the method of K2012 [Kharchenko et al., 2012], we can assign a kinematic probability for each star within a cluster, according to Equation 2.2.6

$$P^i_{kin} = -\frac{1}{4}\left[\left(\frac{\mu^i_x - \overline{\mu_x}}{\varepsilon_{\mu^i}}\right)^2 + \left(\frac{\mu^i_y - \overline{\mu_y}}{\varepsilon_{\mu^i}}\right)^2\right] \tag{2.2.6}$$

where μ^i_x is the proper motion of an individual star for right ascension, μ^i_y is the proper motion for declination and $\overline{\mu}$ is the average proper motion of the cluster. $\overline{\mu}$ is a value taken from literature. Further, following the methods of K2012, the proper motion error, ε_{μ^i}, was set to 1.5 mas/yr for each star - in both RA and DEC- that had a error lower than this, else Gaia archive values were used.

Distance Probabilities

The distance for each star within the cluster was calculated using

$$\text{distance (pc)} = \frac{1}{\varpi} \tag{2.2.7}$$

where ϖ is the Gaia parallax of each star in the cluster. Although parallax is always positive, due to experimental uncertainties some stars have negative parallax in the downloaded tables of data. To remove this error, parallax was limited to positive values only. In addition, the distance range was limited to ±400 parsecs from the lower and upper limits of current estimates of distance from literature for each cluster, except R147 which has an estimated distance of 300 pc so the boundaries were ±50 pc. Following this, the distances of the stars within the clusters were fitted with a Gaussian distribution, using the python package `Astropy`

$$f(x) = Ae^{\frac{-(x-x_0)^2}{2\sigma^2}} \tag{2.2.8}$$

where A is the amplitude of the function, and x is the value of a data point, in this case, the distance of a star. The mean and standard deviations were then determined using values from the fitted data sets and were used to assign a probability to each star within the cluster. Figure 2.3 shows the histograms of the distances for each cluster and the fitted Gaussian curve. Table 2.4 displays the distance values derived for the three selected clusters using the Gaussian fits.

Table 2.4: The mean distance and the standard deviation of each cluster data set and the parameters derived using the Gaussian fit.

Name	Mean distance (pc)		Standard Deviation (pc)	
	Dataset	Derived	Dataset	Derived
M67	842	873	153	73
R147	306	322	26	49
NGC 2158	4525	3257	2949	2972

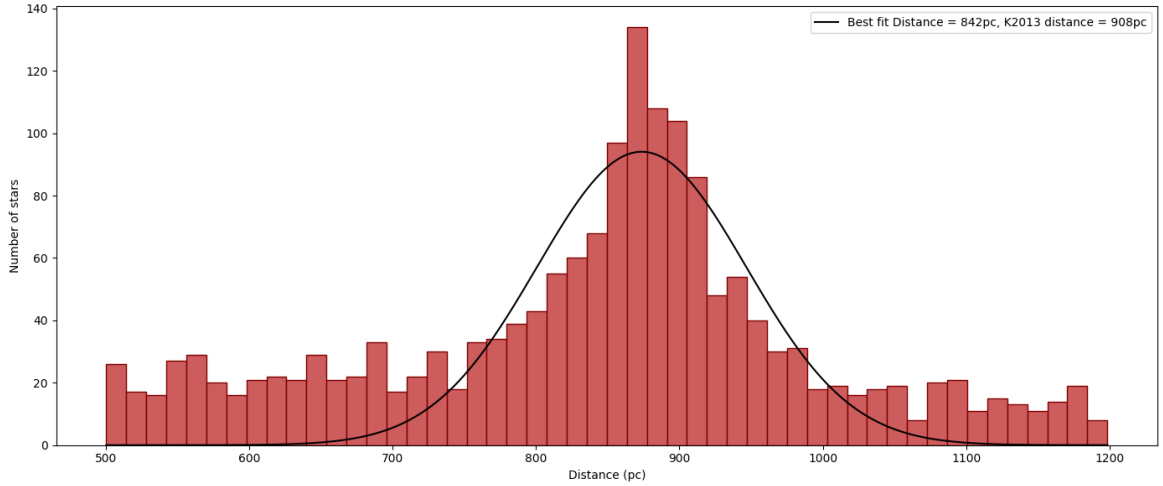

(a)

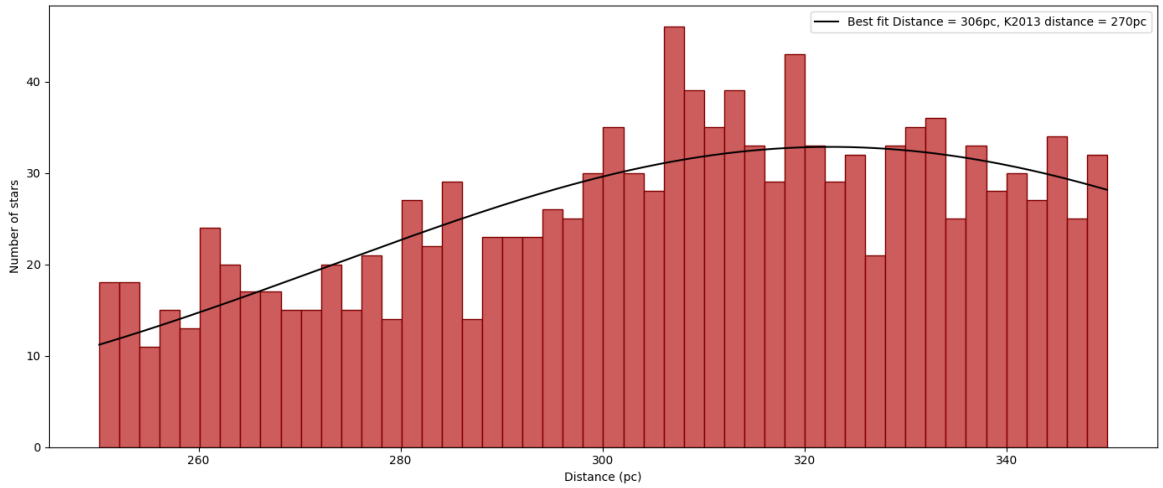

(b)

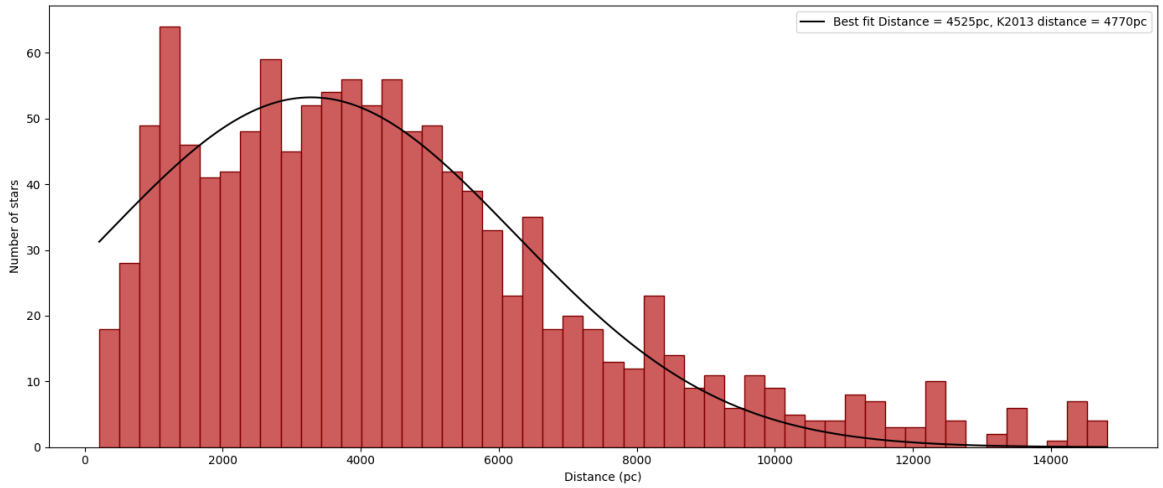

(c)

Figure 2.3: Histogram of the distance distribution for the stars in each cluster (red bars) and the Gaussian fit (black) for (a) M67, (b) R147 and (c) NGC 2158.

Following the fitting of the Gaussian to the distance distribution for each cluster, each star in each cluster was assigned a distance probability. The Z score is a measure of how many standard deviations below or above the population mean a data point is. This was calculated for each of the stars using

$$Z = \frac{x - \mu}{\sigma} \tag{2.2.9}$$

The mean and standard deviation used to calculated the Z score were the values derived from the Gaussian fitting. Using this Z score, a cut was made for all stars that were not within 2σ. The probability was assigned using the python package `SciPy` [Jones et al., 2001].

Total probabilities

Total probabilities were computed by calculating $P_{total} = P_{kinetic} \times P_{distance}$. The threshold for membership was set using 2σ standard deviation for each cluster.

Radial profile

In 1962, King introduces three spatial parameters, r_c (core radius), r_t (tidal radius) and k (normalisation factor) [King, 1962]. The tidal radius for an open cluster is approximately the size of the cluster and the normalisation factor is the background stellar density [Piskunov et al., 2007]. King also modelled the density profiles of globular clusters. This model has been applied to open clusters to determine their radial profiles. Our clusters were fitted using a similar profile, shown in Equation 2.2.10.

$$f(x) = k \, \frac{r_c}{1 + \left(\frac{r_t}{r_c}\right)^2} \tag{2.2.10}$$

We plot stellar density as a function of radius and when the stellar density of the cluster is approximately equal to background stellar density (k), that is the apparent size of the cluster. The graphs for radial profiles are included in the results section for each cluster.

2.2.2 Cluster Membership Results: M67

Messier 67 (NGC 2682) is an open cluster with a reported distance of 800 - 900 parsecs [Stello et al., 2016, Bellini et al., 2010] and is approximately solar age (estimated age of 4 Gyrs) with solar metallicity [Barnes et al., 2016]. M67 is red giant rich and well researched, hence an ideal target to confirm our methodology. The initial values for the proper motion in RA and DEC (μ_x^i, μ_y^i) used to calculate kinematic probability were taken from Bellini et al. [2010]. Table 2.5 shows the values for proper motions, distance, 2σ members and apparent size derived from this work in comparison with three literature values. The number of stars in the cluster varies slightly with different data sets taken from various telescopes with differing sensitivity. The red giant branch (RGB) is distinct on the Colour Magnitude Diagram (CMD) - also known as HR diagrams (discussed in Section 1.1.3) and is one of the ways of classifying stars. Others criteria for classification include metallicity, temperature, and radial velocities. Stello et al 2016 (hereafter S2016) is a comprehensive study of the dynamics of this cluster, including an asteroseismic analysis of the RG members with detailed properties of each star.

Table 2.5: Properties of M67 obtained by this work and compared with three recent studies.

Cluster Parameter	This work	S2016	K2013	Bellini et al. (2010)
Distance (pc)	876	816 ± 11	890	-
Members (2σ)	540	-	637	-
Number of RGs	29	32	-	-
Apparent size	27’	26’5”	33’	-
Proper motions RA (μ_x^i)	-11.0	-	-7.31	-9.6 ± 1.1
Proper motions DEC (μ_y^i)	-3.0	-	-5.92	-3.7± 0.8

Figure 2.4a shows the CMD of all the stars in the visible field for M67, and Figure 2.4b shows the CMD after the analysis. The RGs in this work were identified using a CMD of M67 as shown in Figure 2.4b, which was produced using the Gaia magnitudes. Figure 2.5 shows a comparison CMD from the Gaia archives; using this we identify that the

analysis has produced an fairly accurate set of cluster parameters. The Gaia CMD is a good comparison to the CMD computed in this study as it has the same magnitudes, and for which the M_G is denoted as G on the plot from this work. Although S2016 do not directly identify members, they cite the members identified by Geller et al. [2015] to be 562; of these S2016 identifies 32 to be RGs. Computed results from this analysis yield 540 members with 29 RGs.

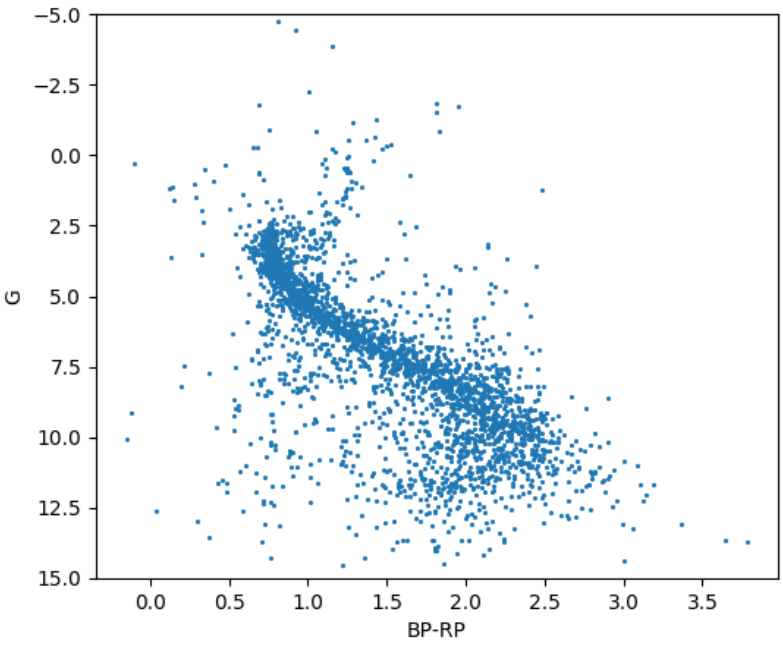

(a)

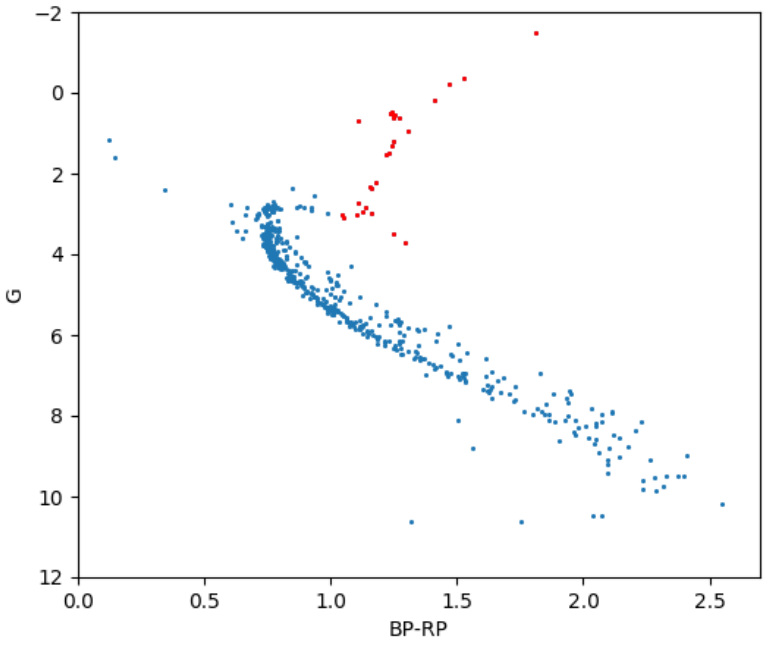

(b)

Figure 2.4: The Gaia CMD of Gaia G magnitude versus Gaia (BP-RP) colour for (a) all the stars in the field before the cluster membership and (b) of cluster members, after analysis where the blue dots indicate the members and the red dots indicate RGs

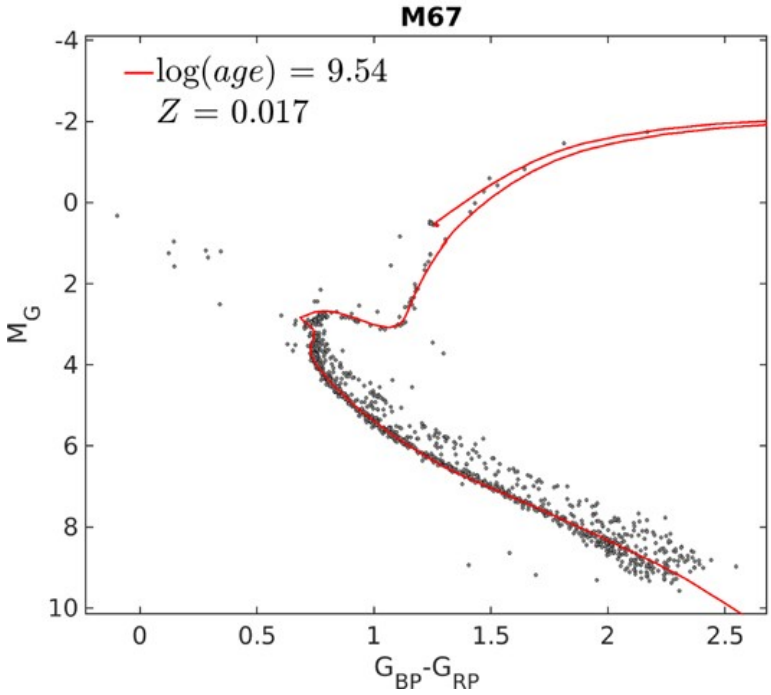

Figure 2.5: CMD of M67 as published by Gaia DR2 [Babusiaux et al., 2018]. Black dots represent the cluster members and the red line is an isochrone fitting which shows the estimated age for this cluster by Gaia archives. Image: Babusiaux et al. [2018]

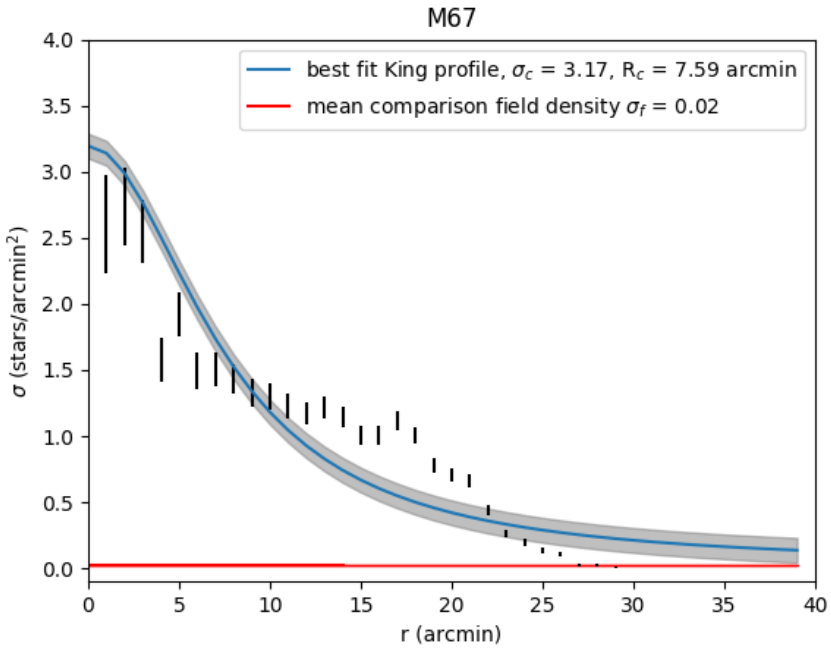

Figure 2.6: Radial profile fitting of the M67, where the blue curve shows the best fit of Kings profile with errors (grey curve), the red line is the background stellar density and the black data points are stars in the field of view. The apparent size for this cluster is 27 arcmins.

2.2.3 Cluster Membership Results: Ruprecht 147

Ruprecht 147 has a number of comprehensive studies [Curtis et al., 2013, Carlberg, 2014]. Curtis et al. [2013] (hereafter C2013) refers to R147 as a 'new benchmark for stellar astrophysics' because of its proximity and age. This mean that this cluster can be used as an example to understand stellar cluster formation and evolution. Their paper can be seen as a updated version of Kharchenko et al. [2005b] as it uses similar methods of proper motion reduction and confirm the results of the 2005 study. C2013 also confirms that R147 contains 81 high confidence members and a further 21 potential members.

Table 2.6 shows the values computed in this study compared to C2013. The major issue with R147 is that its apparent size is 1.25°. Such a large cluster apparent size results in a higher degree of contamination from foreground and background stars and

hence it is easy to obtain incorrect proper motions, a problem faced in papers such as Dias et al. [2006]. We adopt the proper motions provided by C2013 to use as initial mean proper motions of the cluster in the kinematic probability analysis [Curtis et al., 2013].

Table 2.6: Comparison of cluster properties between this study, C2013 and K2013.

Cluster Parameter	This study	C2013	K2013
Distance (pc)	322 ± 24	300	270
Members (2σ)	96	81	49
Number of RGs	7	11	-
Apparent size	1° 13'	1° 15'	33'
RA Proper motion	-0.91	-1.1	-1.59
DEC Proper motion	-26.76	-27.7	-28.04

As this cluster is close to us this meant the distance window had to be narrow, hence we use ± 50 pc for this cluster. Selection of RGs was done by analysing the CMD for the cluster. C2013 identify 11 RGs out of the 81 high confidence members. We identify 7 RGs within 2σ of the total probability. This confirms to a sufficient degree that the memberships derived in this work are accurate and can be used in further analysis of RGs. We computed distance, membership, apparent size and proper motions using kinematic and distance probabilities for R147 in a similar way to our analysis for M67. Figure 2.7a shows the CMD of stars in the visible field of 1.87° and Figure 2.7b shows the CMD of the cluster members after the analysis. Once the final RGs members were determined, the RA and DEC of each star was used to find the Kepler K2 identification numbers.

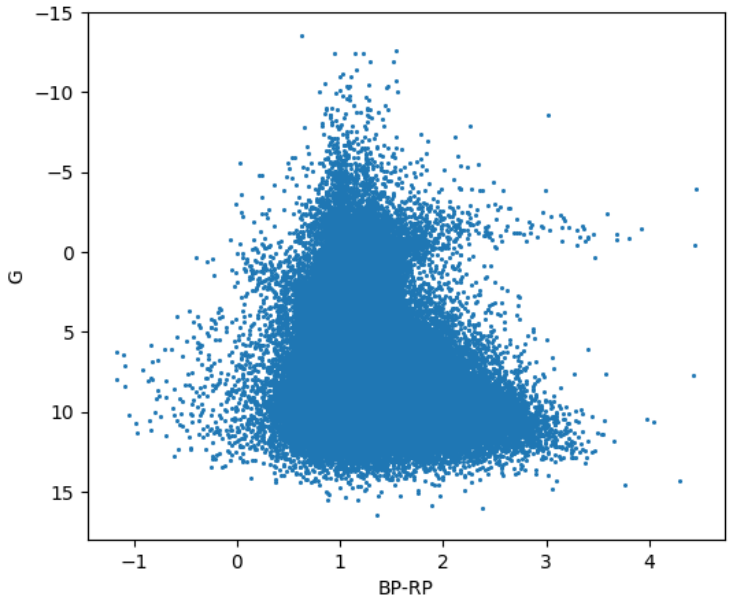

(a)

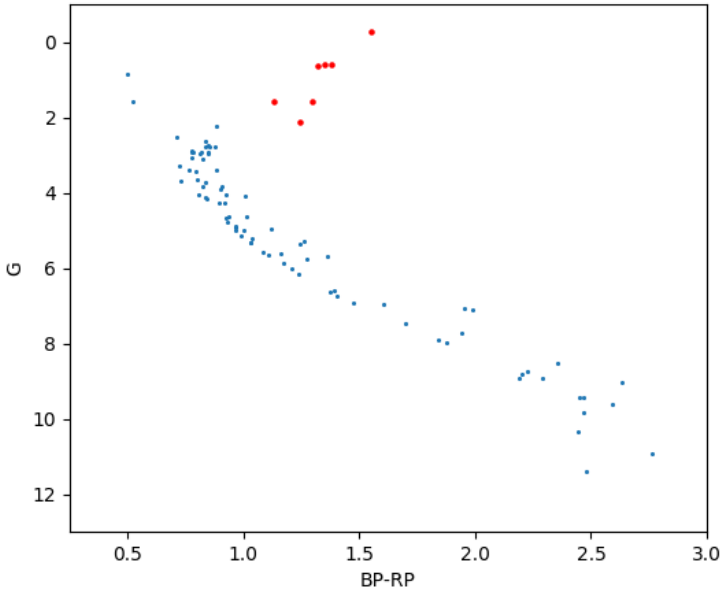

(b)

Figure 2.7: The Gaia CMD of Gaia G magnitude versus Gaia (BP-RP) colour for (a) all the stars in the field of view and (b) the members obtained after the analysis. The blue dots are members and the red dots are RG members.

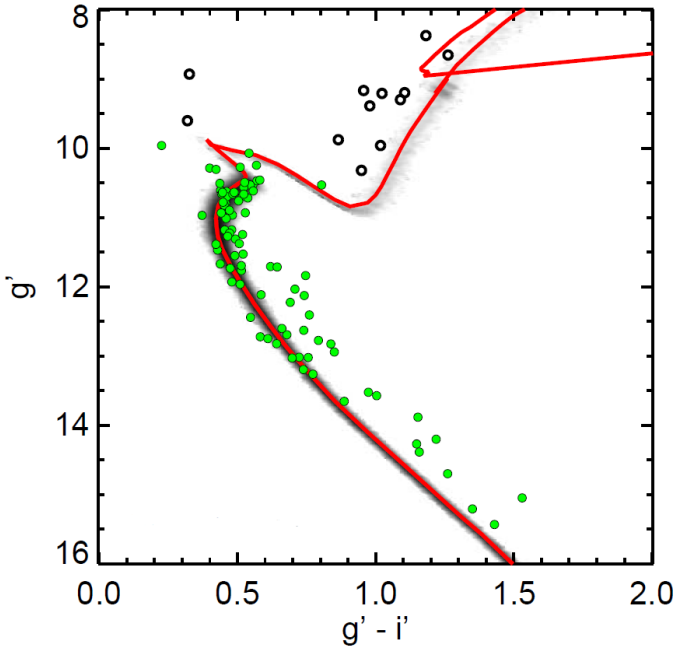

Figure 2.8: CMD from C2013 as a comparison to the CMD from this work. These are comparable even though C2013 uses data from different bands and hence their CMD is g'-i' vs g'. Image: Curtis et al. [2013]

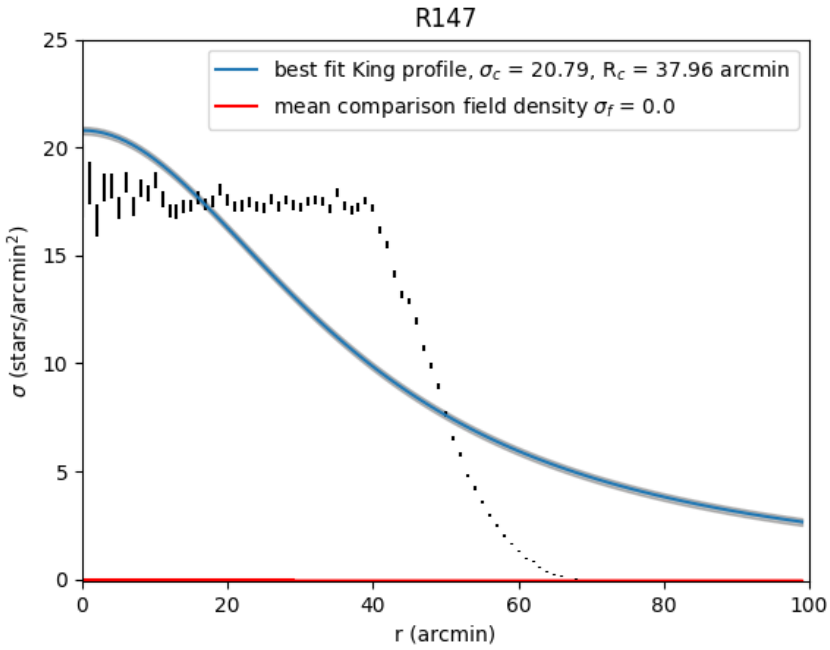

Figure 2.9: Radial profile fitting of the R147, where the blue curve shows the best fit of Kings profile with errors (grey curve), the red line is the background stellar density and the black data points are stars in the field of view. The apparent size for this cluster is 68 arcmins.

2.2.4 Cluster Membership Results: NGC 2158

Unlike its neighbouring cluster M35, NGC 2158 is not well studied and has few detailed publications. Its proximity to M35 in the sky makes it difficult to determine accurate parameters for this much more distant cluster. There is currently no agreement on the cluster's age, estimates range from 0.8 Gyrs [Arp and Cuffey, 1962] to 2 Gyrs [Carraro et al., 2002]. We adapt from K2013 which estimates the age of the cluster to be 2.13 Gyrs [Kharchenko et al., 2013]. Carraro et al. [2002] confirms that this cluster is a member of the old thin-disk population of our Galaxy. The membership for this cluster is also not well established; there is only one study, K2013, which determines the number of members to be 364. However there are multiple CMDs available which can be used to cross-check the derived CMD for members in this work. Our study determines a cluster membership of 338 with 11 being RGs.

2.2. Cluster Membership

Figure 2.10a shows the CMD of all the Gaia data downloaded for NGC 2158, and Figure 2.7b shows the CMD of the members determined after the analysis. We also compare these with a CMD from Christian et al. (1985) to check the accuracy of the results. Determining the distance to this cluster was challenging as the range of estimates is more than 1000 parsecs. Table 2.7 shows the comparison between the calculated parameters from this study with literature values for the basic cluster parameters.

Table 2.7: Cluster parameters for NGC 2158 derived in this study compared to values from two other publications. (*) indicates values which were used in the paper; however, they are a derivation of Kharchenko et al. [1997]

Cluster Parameter	This work	Carraro et al. (2002)	K2013
Distance (pc)	3535 ± 1236	3600 ± 400	4770
Members (2σ)	338	-	364
Number of RGs	11	-	-
Apparent size	6’	5’	8’24”
RA Proper motion	0.086	-0.66* ± 2.03	-7.31
DEC Proper motion	-2.186	-3.23* ± 2.16	-2.48

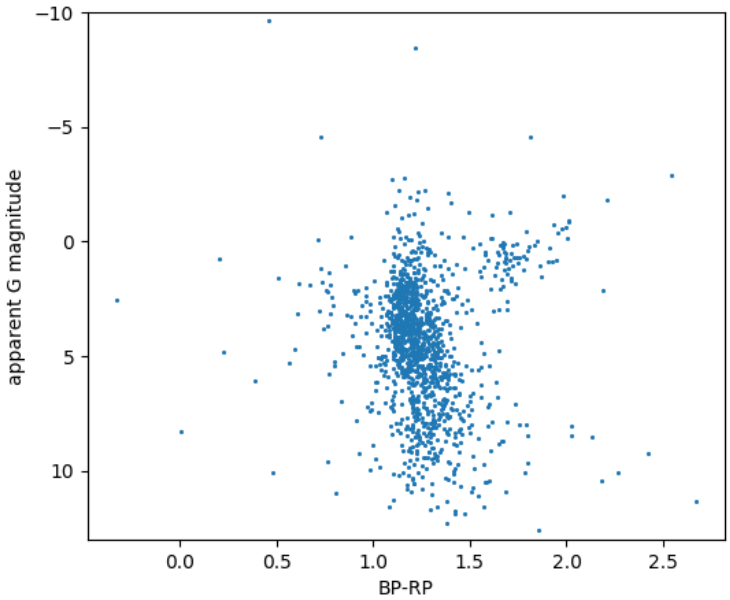

(a)

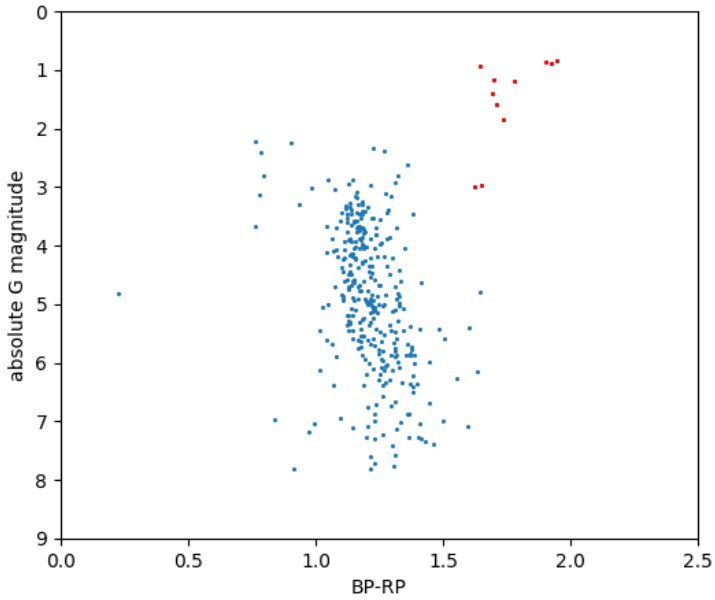

(b)

Figure 2.10: CMD of (a) all the stars in the field of view and (b) members of NGC 2158 after analysis. The red dots are the RGs while the blue dots are all other cluster members.

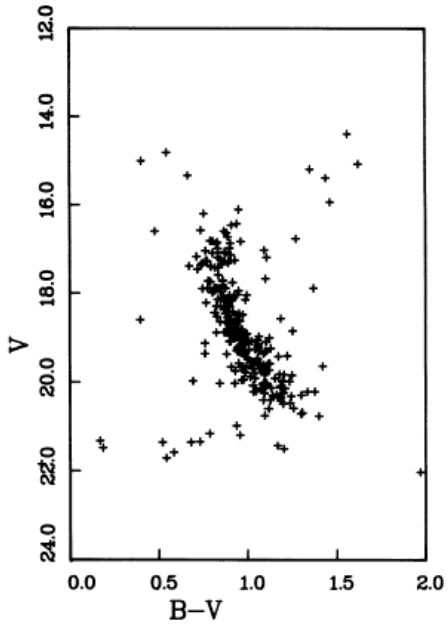

Figure 2.11: Comparison CMD for NGC 2158 from the publication Christian et al. [1985]. They have used data from the V and B band, hence the plot is V-B vs V, however this is still comparable to our CMD. Image: Christian et al. [1985]

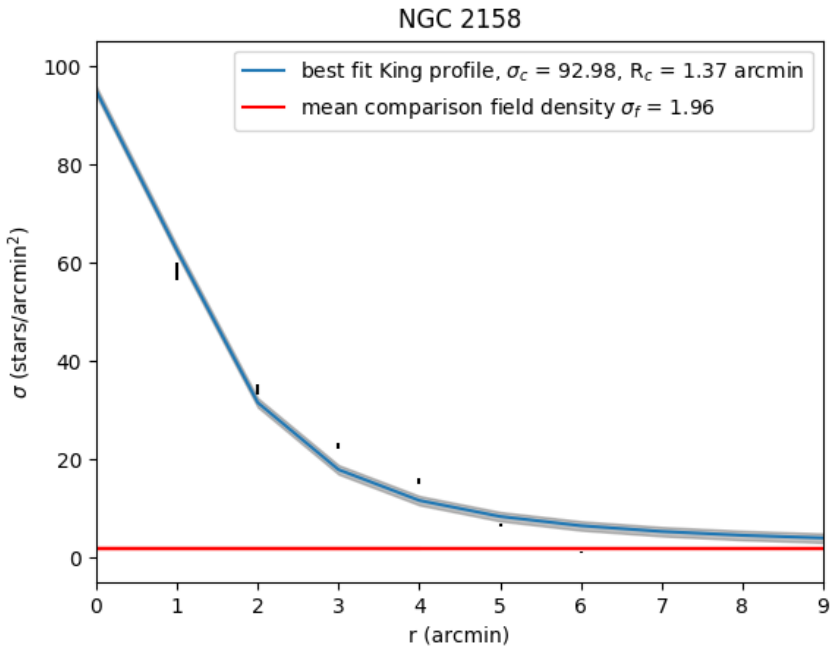

Figure 2.12: Radial profile fitting of the NGC 2158, where the blue curve shows the best fit of Kings profile with errors (grey curve), the red line is the background stellar density and the black data points are stars in the field of view. The apparent size for this cluster is 6 arcmins.

2.2.5 Resulting RGs

Once the final RG members were determined, the RA and DEC of each star was used to find the Kepler K2 identification numbers for all cluster. Table 2.8 and 2.9 list the RGs with their K2 ID, RA and DEC. The tables are a combination of RGs found in the membership study above, S2016 for M67 and C2013 for R147. Although there is K2 data for NGC 2158, there are only 40 observed targets (compared to a possible 338 identified in the membership study in Chapter 2) and none are identified as RGs. Hence, NGC 2158 is not analysed any further. C2017 selects RG targets with the condition that they have a maximum frequency greater than $50\mu Hz$, we use the ν_{max} given in S2016 as an indication of which RGs we select for asteroseismic analysis, which results in a total of 17 RGs. We do not have this information for the stars in R147 and hence we use all the RGs found.

Table 2.8: Identified RGs (by this study and S2016) in M67, with a maximum frequency greater than 50 μHz

K2 ID (EPIC ID)	Right Ascension	Declination
211413623 (200200535)	08 51 16.761	+11 50 49.69
211396385	08 50 49.650	+11 35 08.93
211414300 (200233344)	08 51 42.539	+11 51 22.90
211408346 (200233404)	08 51 21.319	+11 46 03.13
211410231 (200200500)	08 51 44.873	+11 47 47.43
211412928 (200233360)	08 51 042.525	+11 50 02.61
211411629 (228682441)	08 51 30.590	+11 48 54.90
211416749	08 51 35.777	+11 53 34.69
211414687	08 51 39.384	+11 51 45.32
211421954	08 51 18.972	+11 58 11.01
211409560	08 51 08.384	+11 47 12.13
211388537	08 52 20.042	+11 27 36.01
211403248	08 52 26.328	+11 41 27.67
211415364	08 50 58.157	+11 52 22.35
211411922	08 50 49.949	+11 49 12.73
211409088	08 51 44.737	+11 46 45.99
211414203	08 51 18.774	+11 51 18.67

Table 2.9: Identified RGs (by this study and C2013) for R147

K2 ID (EPIC ID)	Right Ascension	Declination
219310397	19 17 03.430	-17 03 13.78
219403368	19 13 48.180	-16 50 06.19
219624547	19 18 09.781	-16 16 22.34
219688088	19 15 26.118	-16 05 57.07
219697419	19 17 23.845	-16 04 24.36
219704882	19 17 11.310	-16 03 08.22
219757320	19 14 02.731	-15 54 05.73

Chapter 3

Asteroseismology

3.1 Light curves and reduction

K2 data is available in many forms and can be downloaded or accessed from various sources. The most common sources are File Transfer Protocol (FTP) servers, K2 search and retrieve and Barbara A. Mikulski Archive for Space Telescopes (MAST). MAST is widely used by the astronomy community as it contains not only the unprocessed data but also has other products which have been produced by publications or catalogues. These products are very useful and are referred to as High Level Science Products (HLSP). Although the HLSP are helpful, they cannot be used for the asteroseismological analysis later in the study as it requires a file of type `KeplerLightCurveFile`. We use two methods to obtain light curves and compare them to literature value to ensure their accuracy. In the following method descriptions, we use 211413623 (20020535), a RG in the M67 cluster, as an example for all reduction and analysis figures. Figures for all other targets can be found in the online repository: tinyurl.com/lcpgall

K2 observes in two cadence modes, short and long. Short cadence has an exposure time of 58.58 seconds which results in better frequency resolution. The long cadence mode has an exposure time of 29.4 minutes [Kinemuchi et al., 2012]. Light curves and Target Pixel Files (TPFs) for all targets were downloaded in long cadence mode, data from all campaigns was downloaded and appended for better frequency resolutions. S2016

recommends using short cadence, however, C2017 uses long cadence for its analysis. As not all targets in R147 had short cadence data available, we use long cadence in this study.

3.1.1 Method A: SAP flux light curves

In this method, the target pixel files are used to extract the flux to produce a light curve. There are currently two python packages available for processing K2 data, `PyKE` or `Lightkurve` - the latter of which was used in this study [Lightkurve Collaboration et al., 2018]. The target pixel file (TPF) contains both an uncalibrated and calibrated postage stamp pixel image. It also contains the target mask, the optimal aperture, and the contamination of background sources. The optimal aperture is the mask used by the *Kepler* pipeline and is a set of pixels. Each pixel has a flux value, the sum of these produces the total flux for the star. The halo pixels, which are the surrounding the target pixels (an example can be seen in Figure 3.1), were used for calibration. The light curve was produced using *Simple Aperture Photometry* (SAP), which is the sum of the pixels contained within the optimal K2 aperture [Kinemuchi et al., 2012]. As this does not account for background source contamination, in each case the TPF was visually assessed to ensure that the aperture mask only contains the desired target. During this assessment, pixels with flux values greater than approximately 5000 photoelectrons per second($e^{-}s^{-1}$) [Barentsen, 2019] were selected for M67 and over 50000 photoelectrons per second($e^{-}s^{-1}$) [Barentsen, 2019]. Figure 3.1 shows a comparison of the K2 pipeline mask and the mask used in this study. As R147 is a very bright cluster, there was concern about the stars being saturated. However, this is not the case and the usability of the data is confirmed by multiple publications, including the SFF pipeline (which generates HLSP) Vanderburg and Johnson [2014] and Torres et al. [2018].

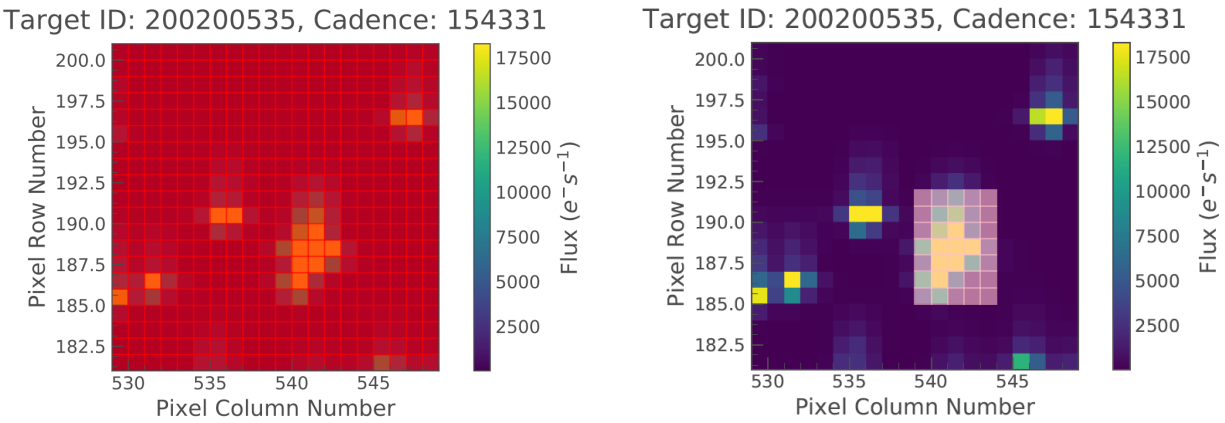

(a) (b)

Figure 3.1: The target pixel file for 211413623 (the brightest and largest collection of pixels is the target), (a) shows the K2 pipeline mask which includes all the background sources, hence contaminating the flux; and (b) shows the manually selected mask which only contains the target.

The light curves made using SAP needed to be corrected for all systematic artefacts and were in all aspects raw. Figure 3.2a shows the raw light curve for 211413623 as an example. One year into the *Kepler* mission, it was found that the motion of the spacecraft affected the signal, which added an artefact in the light curves. The artefact was that the observations were not correlated with the *Kepler* flux time series and need to be corrected; the corrections are provided by *Kepler* as linear combinations of orthonormal functions, called Co-trending Basis Vectors (CBVs) [Christiansen et al., 2013]. K2 releases the 16 most common trends for each channel per campaign. This correction was rather challenging as the trends are unique for each target and must be manually fitted and removed. This correction was carried out in Python using the package `Lightkurve`, which fits the light curve with the trends from the campaign the target was observed in. Figure 3.2b shows the first 8 common trends for a 211413623 as an example. Correcting for all 16 trends would have risked potentially over-correcting and possibly losing astrophysical signal, hence the light curves were only corrected for the first 8 trends, as recommended by most literature including `Lightkurve` [Lightkurve Collaboration et al., 2018]. Figure 3.2c shows the same light curve after the trends have been removed. A comparison between the light curve in Figure 3.2a

and Figure 3.2c shows negligible difference; however, other stellar light curves show significant differences after de-trending.

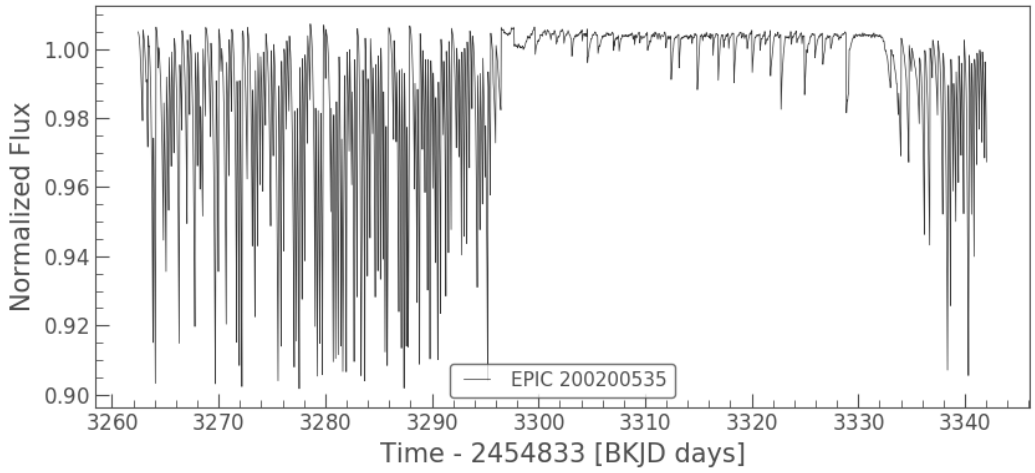

(a)

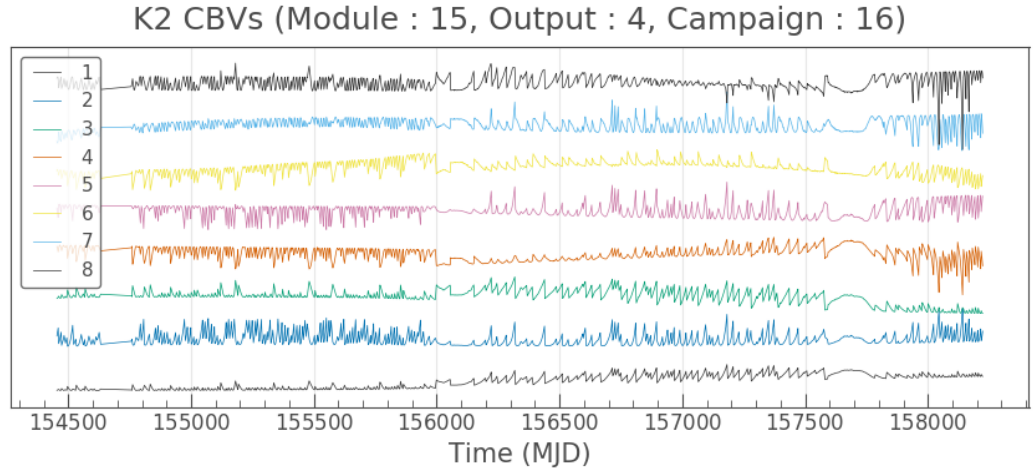

(b)

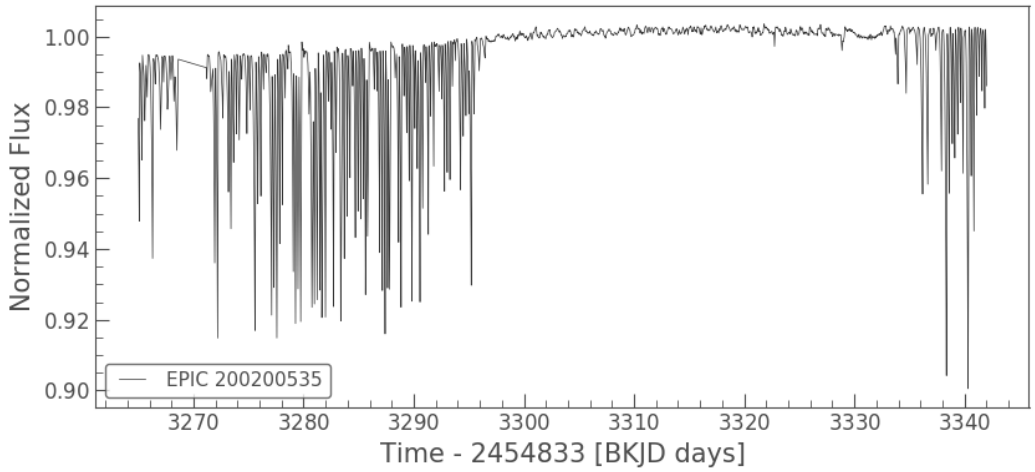

(c)

Figure 3.2: (a)Unprocessed light curve for 2111413623 extracted from TPFs. (b) The first 8 trends fitted for this light curve for 211413623, using the CBVs provided by the K2 archives. (c) Light curve for 211413623 after CBV correction

3.1.2 Method B: PDC flux light curves

Data was downloaded for all the targets, using the K2 servers, in the form of KeplerLightcurve files. These files contain: SAP flux (discussed in Method A); the Pre-Search Data Conditioning Simple Aperture Photometry (PDCSAP; PDC henceforth) flux, and *Kepler*telescope artefact information. In this method (Method B), we used the PDC flux to create light curves. The PDC pipeline is always in development to improve the de-trending algorithm and is designed to remove system artefacts [Kinemuchi et al., 2012]. It uses CBV corrections to maximise the astrophysical signal by fitting the trends for that campaign to the SAP flux [Kinemuchi et al., 2012]. Although this is similar to Method A, the fitting of CBVs for each light curve is not unique in this case. The pipeline also corrects excess flux by de-selecting the unnecessary flux from background sources and removes outliers around a set median. As well as this, the pipeline flags and removes any discrete discontinuities in the data which are a result of space craft activity; both planned (such as Earth point downlinks) and unplanned (for example, loss of fine pointing) [Christiansen et al., 2013]. The disadvantages to using this pipeline are: the correct discontinuity specific to the source may not be identified; incorrect de-trending may introduce more noise; and positive outliers may be removed if not correctly flagged. Figure 3.3 shows the PDC flux with the SAP flux in the background for 211413623.

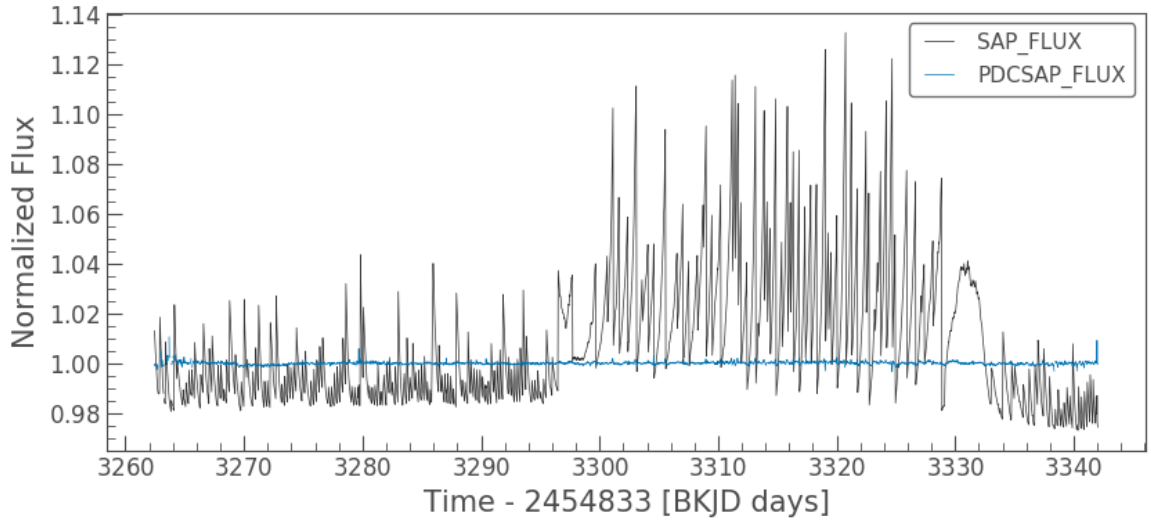

Figure 3.3: Light curve produced using the PDC flux (blue line), with the SAP light curve in the background (black line).

3.1.3 Self-Flat Fielding

Light curves obtained from both; Methods A and B, needed to be further corrected for telescope systematic errors. The most popular method currently used to perform this correction was established by Andrew Vanderburg in 2014, called the 'Self-Flat Fielding' (SFF) [Vanderburg and Johnson, 2014]. The SFF method was developed specifically for K2, since the original telescope lost its two wheels which reduced the photometric precision. This method corrects for artefacts caused by the instability of the spacecraft [Vanderburg and Johnson, 2014]. The first step was to exclude all data from the first 2.5 days (at the beginning of the mission) as this was when the Two-Wheeled Concept Engineering Test was performed to ensure that the spacecraft was still capable of adequate fine pointing [Vanderburg and Johnson, 2014]. The next step was to exclude all the points that have been labelled as poor quality by the *Kepler* pipeline. These exclusions could only be applied to Method A as the light curves used in Method B does not contain the `QUALITY` flags. Only data points with non-zero quality flags were included in the analysis. Then using the Python package `Lightkurve` the light curve was corrected for SFF, using the correcting module `Corrector(sff)`. For more details on the SFF method, see [Vanderburg and Johnson, 2014]. Figures

3.4a and 3.4b show the SFF-corrected light curves for 211413623 for Methods A and B, respectively. The SFF method is designed to restore the median precision of K2 to a certain degree in comparison to *Kepler* data and it improves K2 data enough so that the science can be continued even after the original *Kepler* mission [Vanderburg and Johnson, 2014].

A comparison of the two light curves does show they are very different. This is due to the reduction being different.

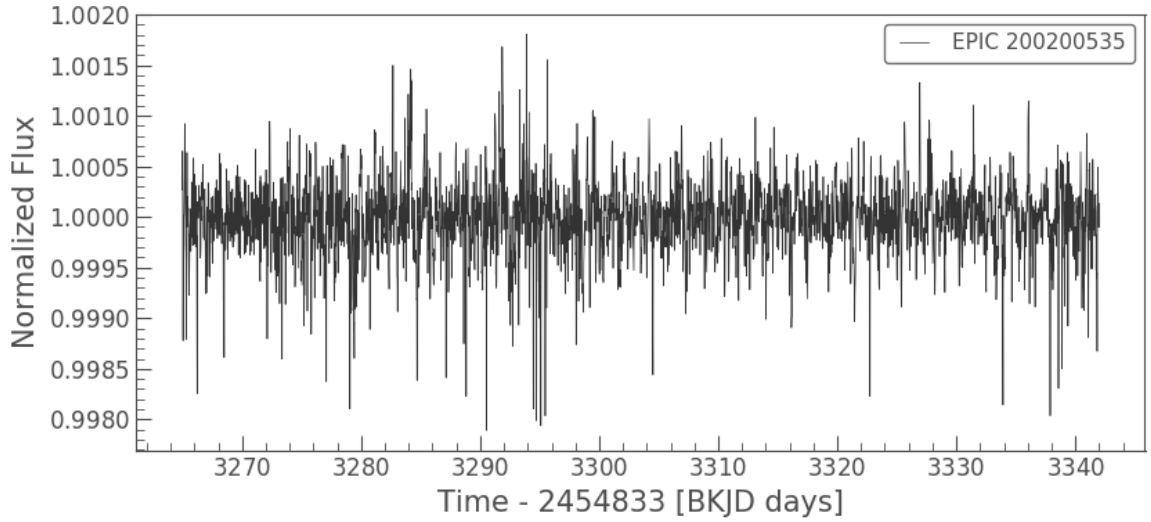

(a)

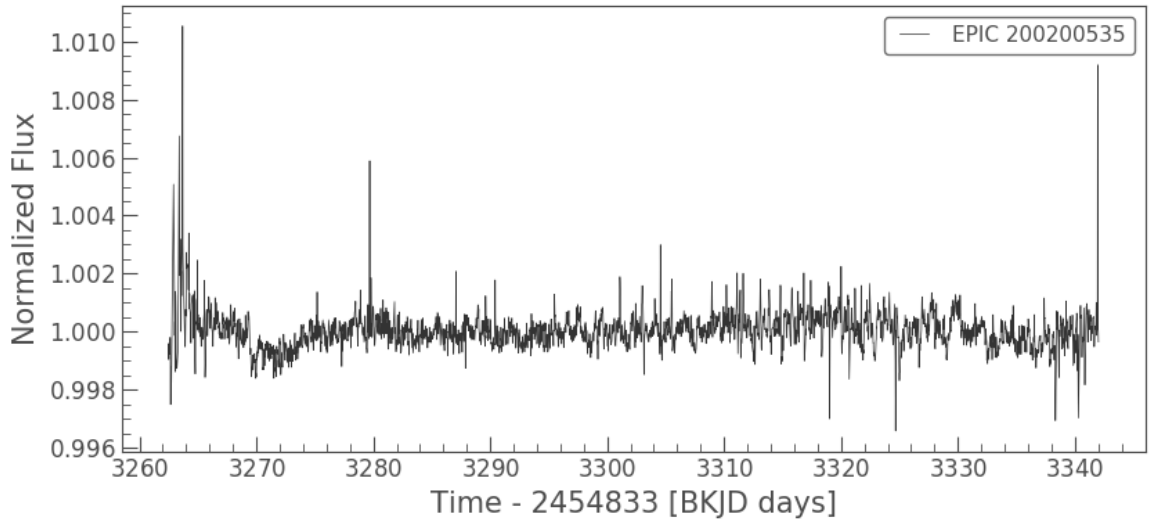

(b)

Figure 3.4: Light curves that have been SFF-corrected (a) for Method A, and (b) for Method B

3.2 Peak bagging

Solar-like oscillations require a unique method for obtaining asteroseismological parameters as their light curves have regular patterns in the peaks. The procedure of fitting and identifying oscillation modes is known as peak bagging. To extract seis-

mic parameters, a Fourier transform of the light curve must be performed to separate astrophysical signals from background noise. As this data is discrete, the traditional Fourier transform cannot be used. Hence, we use non-Fourier-periodograms to search for periods in an unevenly spaced data set [Aerts et al., 2010]. The periodogram for solar-like oscillations has a Gaussian-like shape which requires a global fitting to obtain the maximum frequency, and maximum frequency separation. The periodogram was made using the Lomb-Scargle method with `Lightkurve`'s module `Seismology`. This module was used for both the peak bagging and the frequency analysis. Figure 3.5 shows the periodogram for 211413623 using the final reduced light curves from Method A and B respectively.

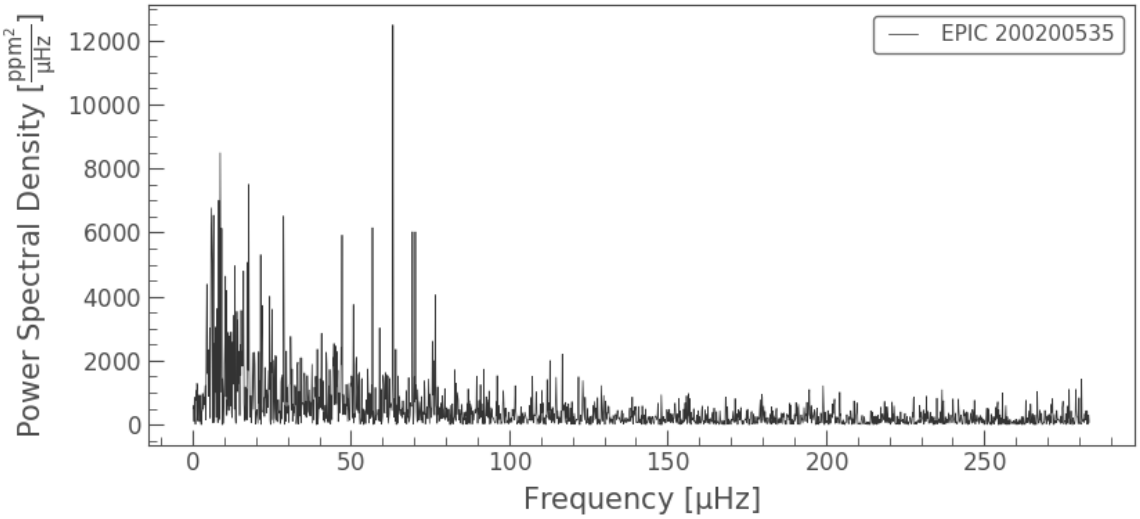

(a)

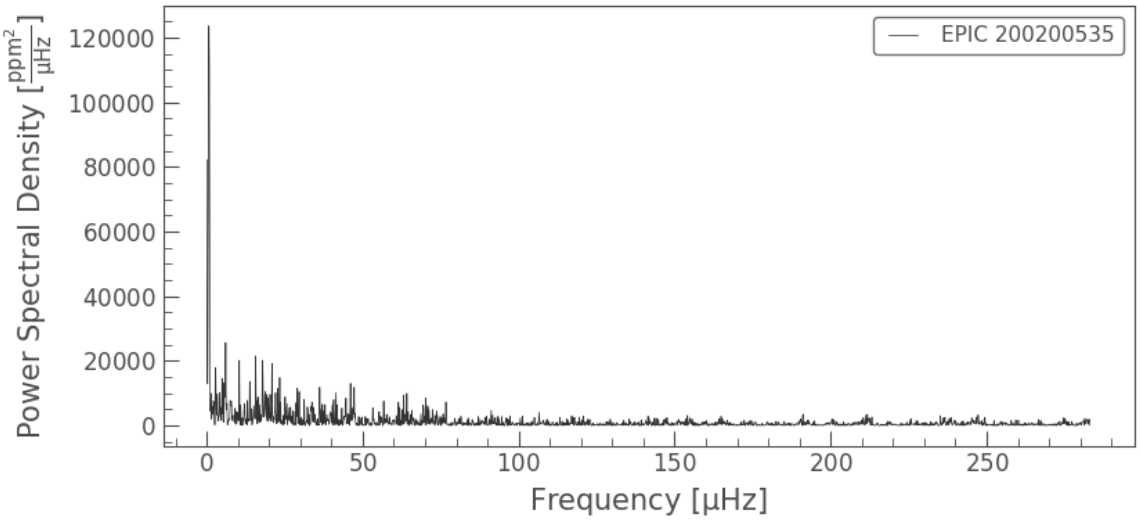

(b)

Figure 3.5: Lomb-Scargle periodograms for 211413623 were made using light curves processed using (a) Method A and (b) Method B. In each case the power spectral density is plotted versus frequency (in microhertz).

Following this, the periodogram needed to be smoothed. This method is used to filter out the noise while conserving the seismic mode peaks, similar to a high pass filter. Smoothing helps eliminate the effects of low-frequency drifts which are often present as a result of with observing instruments or originating from the star. The low-frequency drift introduces background noise which reduces the signal to noise ratio.

The mathematical description of smoothing is that the signal function $x(t)$ is convolved with the a weighting function $w(t)$ as shown in Equation 3.2.1.

$$x_{low}(t) = x(t) * w(t) \tag{3.2.1}$$

Smoothing of the periodogram was done using the `.smooth()` function, shown in Figure 3.6, Method A (Figure 3.6a) and B (Figure 3.6b). This function smooths the periodogram (also known as power spectrum) using the 'boxkernel' method, where the spectra is convolved with a numpy `Box1DKernel` method with a width of `filter_width`, which is in units of frequency.

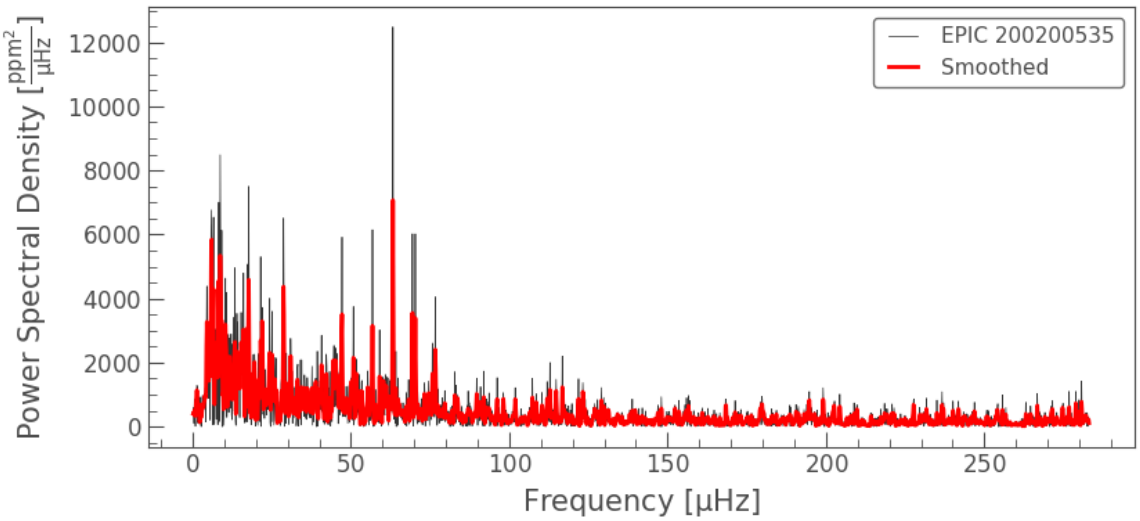

(a)

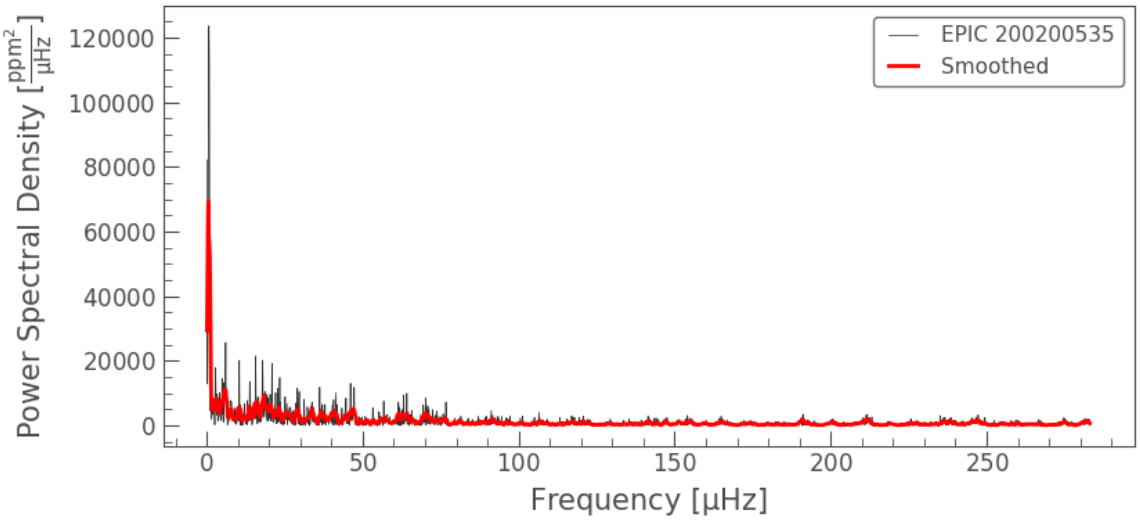

(b)

Figure 3.6: Smoothed (red) power spectra of the light curves for 211413623 cleaned using (a) Method A and (b) Method B, with the Lomb-Scargle periodogram in the background (black)

Following this the periodogram was flattened using `flatten()`. This function divides the periodogram by the smoothed periodogram using a method called `Log Median`. In this script, a moving median across the periodogram is used to estimate the background noise, where the stepsize is determined from:

$$log_{10}(x_0) + 0.5 \times filter\_width \tag{3.2.2}$$

This results in a power spectrum without units, and is referred to as the Signal-To-Noise (SNR) spectrum. This new spectrum can be seen in Figure 3.7, for star 2113413623, Method A and B respectively.

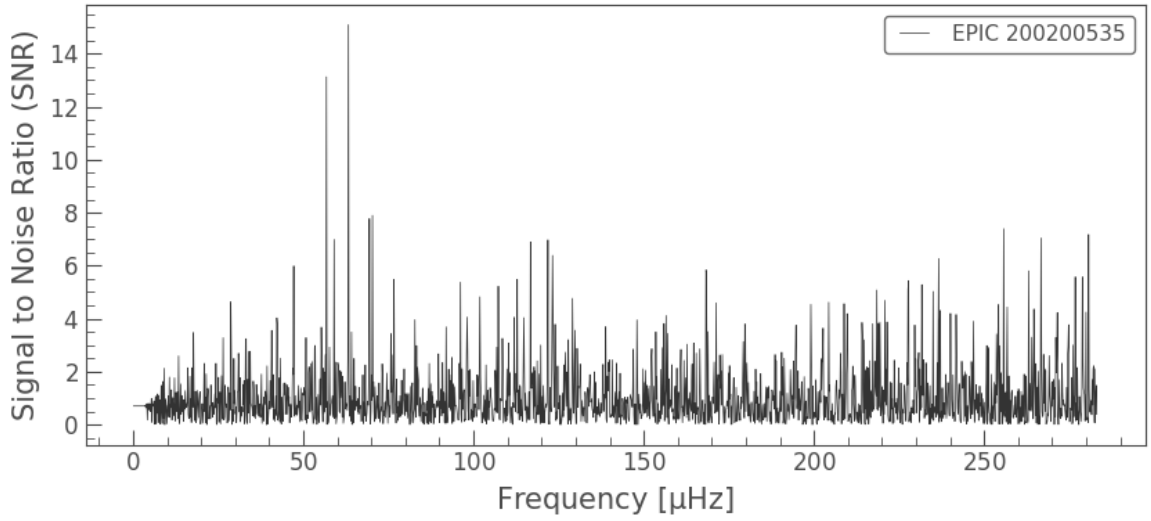

(a)

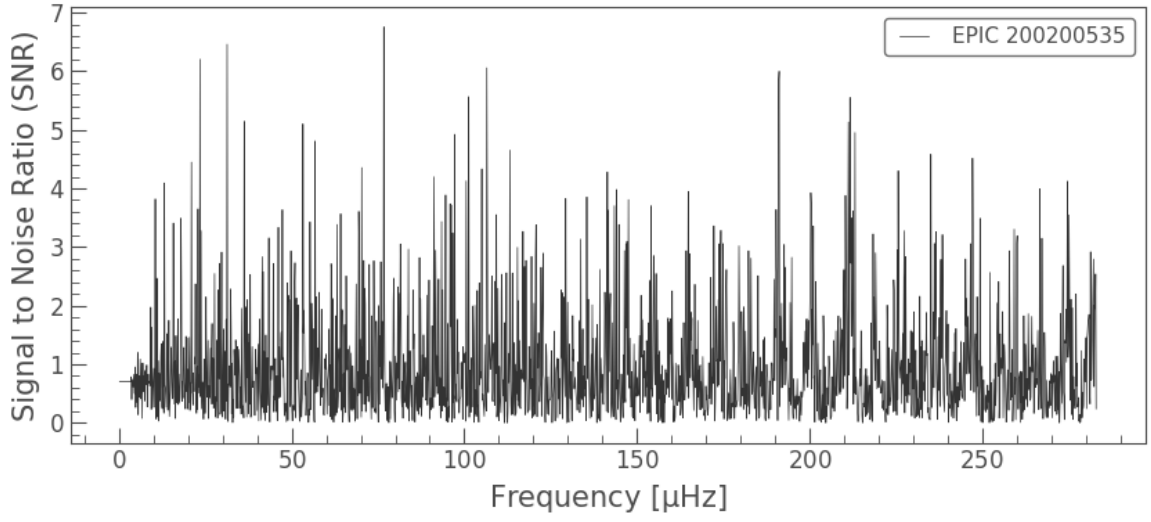

(b)

Figure 3.7: Flattened periodograms for star 211413623, made light curves processed using (a) Method A and (b) Method B

Next, the astroseismic parameters were estimated using the `seismology` module. The first parameter to be estimated is the maximum frequency (ν_{max}), this can be found using `estimate_numax` function. This function uses the autocorrelate function 2D (acf2d) method, which is based on the publication Viani et al. [2019].
The default fixed width is 25 μHz of the window and the frequency window moves in steps of 1 μHz to evaluate the autocorrelation at each step [Lightkurve Collaboration et al., 2018]. The correlation is given using Equation 3.2.3, and the total correlation is given by $C = sum(s^*s)$, where s is a window of the signal-to-noise ratio (flattened) spectrum [Lightkurve Collaboration et al., 2018].

$$C[x, y] = sum(x^* conjugate(y)) \tag{3.2.3}$$

This function is intended for RGs or solar-like oscillations and is unreliable for low signal-to-noise ratios. The same correlation function was also be applied to estimate the frequency separation $\Delta\nu$. Another useful function in the `Lightkurve-seismology` module is the `diagnose()` function which shows a detailed description of how ν_{max} and $\Delta\nu$ are calculated. The repeating correlation produces a lag in the frequency, the first two frequency lag bins are excluded, to make the relevant feature on the plot clearer.Figures 3.8 and 3.9 show the ν_{max} diagnostics and for $\Delta\nu$ diagnosis respectively as an example for target 21143623 (Method A). Plotting the frequency lag vs central frequency produces the plot shown in the middle panel in Figure 3.8. The bottom panel in Figure 3.8 shows the correlation metric plotted vs central frequency, this shows a clear peak where ν_{max} is. The correlation is not as clean as it would be for *Kepler* data, as K2 frequency resolution is much lower as a result of the loss of fine pointing and the time period over which observations were obtained and the cadence of the data.

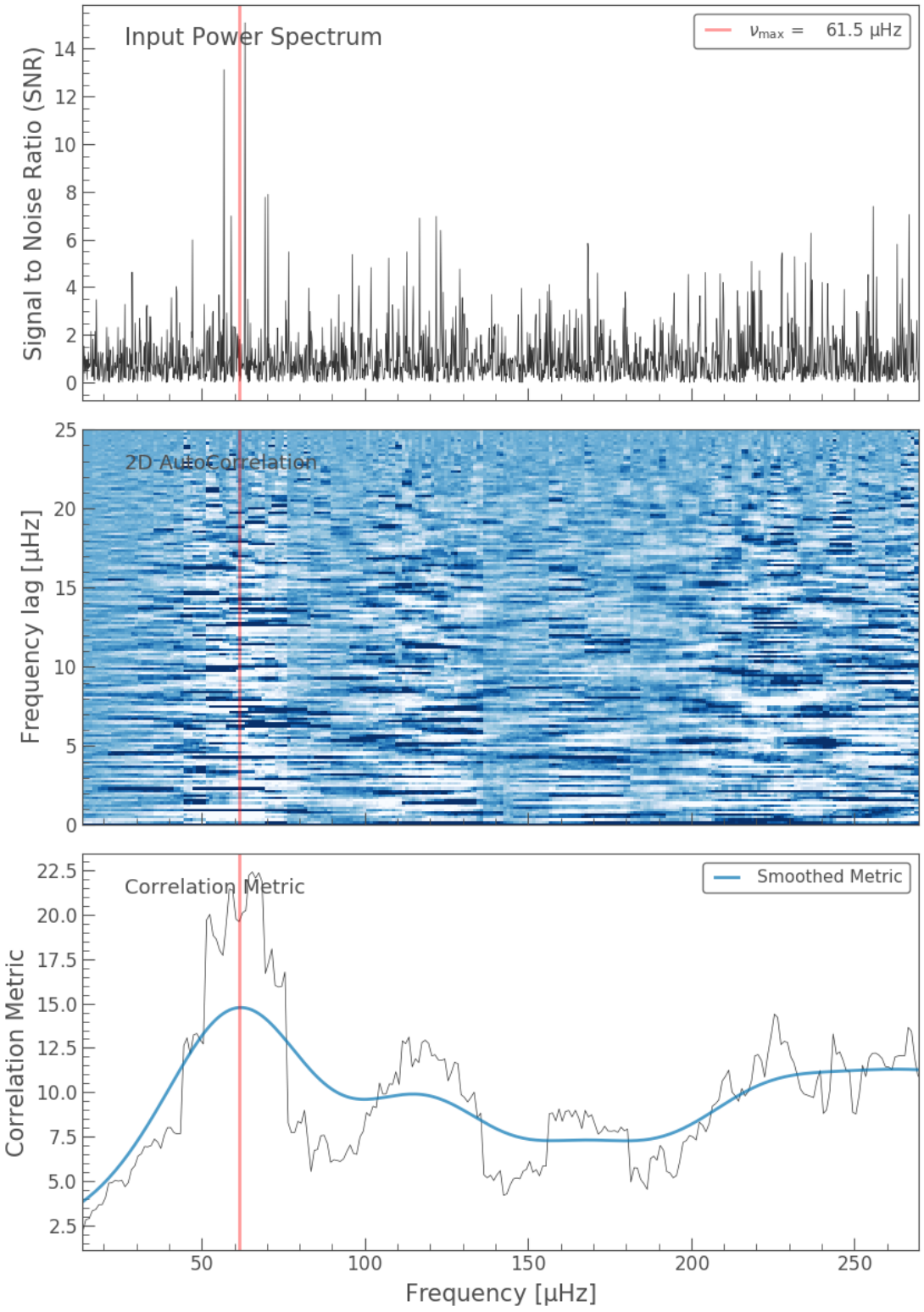

Figure 3.8: ν_{max} diagnosis of 211413623 for Method A. Top: shows the input SNR spectrum. Middle: show the frequency vs the frequency lag. Bottom: shows the correlation metric plotted against the central frequency which shows the ν_{max} (also highlighted by a red line through all the panels).

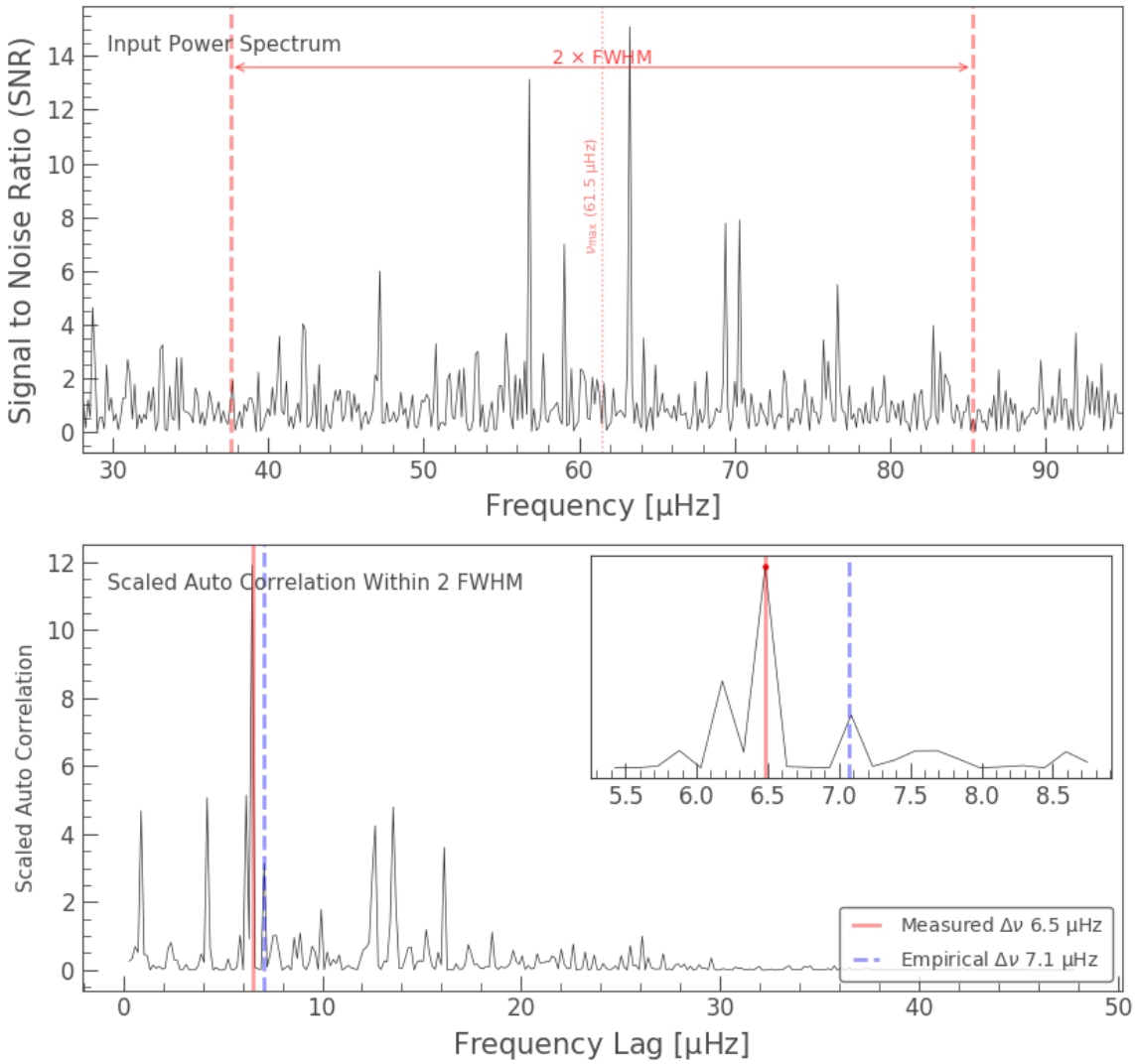

Figure 3.9: $\Delta\nu$ diagnosis of 211413623 for Method A. Top: Bottom:

Once the $\Delta\nu$ and ν_{max} have been found, these can be used to make an échelle plot. Échelle diagrams are made by plotting the frequency modulo ($\nu/\Delta\nu$) against ν. This diagram was first introduced in 1983 by Greg et al. (1983) for helioseismology and is now commonly used in finding the oscillation frequencies in all types of asteroseismological analyses [Bedding and Kjeldsen, 2010]. The diagram is made by splitting the oscillation spectrum into sections of frequency of length $\Delta\nu_{nl}$, which are then stacked, in ascending order of frequency. Échelle plots usually show l modes, but, in this case, the poor frequency resolution of K2 means the modes cannot be identified to sufficient accuracy [Stello et al., 2016]. Figures 3.10a and 3.10b show the échelle plot for 211413623. Figures 3.10c and 3.10d show the échelle diagram of a star from R147 to

demonstrate how these plots vary with each star.

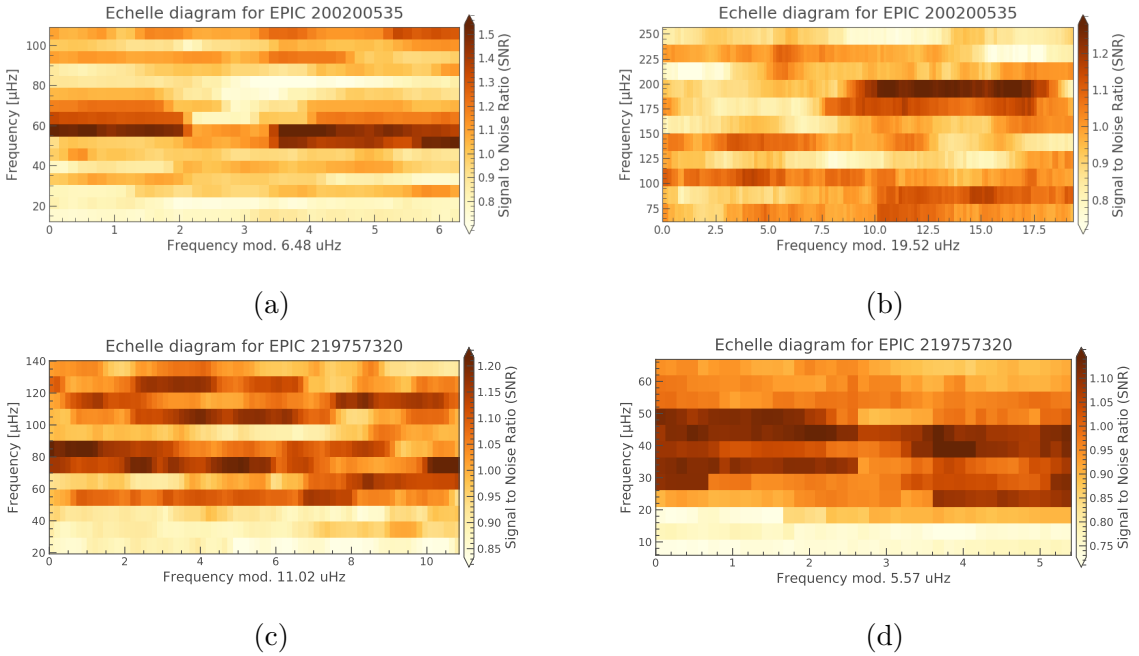

Figure 3.10: (a) and (b) show échelle diagrams for a star (211413623) in the M67 cluster, Method A and B, respectively. (c) and (d) show the diagram for a star (219757320) in R147, for Method A and B respectively.

3.3 Resulting parameters

Using the scaling relations method discussed in Section 1.2.1 the mass, radius and surface gravity (log g) was estimated. The `seismology` module in `Lightkurve` uses the effective temperature $T_{\rm eff}$, $\Delta\nu$ and ν_{max} to determine the former parameters. $T_{\rm eff}$ for all M67 stars (except 211411629 - due to unavailability) were taken from S2016. These are listed in Table 3.3 in Section 3.3. For all other stars, the average $T_{\rm eff}$ of a RG (4800K) was used as no literature values were available.

The results from the methods above are presented and discussed in this section. Tables 3.1 and 3.2 list the properties for each star in the M67 cluster. Table 3.4 and 3.5 display the resulting properties for the RGs in R147. As a comparison of properties of RGs in M67, a table from S2016 is also included (Table 3.3). As $T_{\rm eff}$ for each star in

M67 was used from S1026, it is only listed in Table 3.3. The comparison of $\Delta\nu$ and ν_{max} values for M67 with S2016 shows that the results from Method A are much more accurate than the results of Method B. This conclusion is also applied to R147; the light curves and periodograms from Method A are reliable and can be used for further analysis. This disparity comes from the light curves and therefore periodograms produced by Method B having significantly more noise. This excess noise is a result of the de-trending not being optimised for the signal of RGs in particular; hence some astrophysical signal may have been lost. Additionally, the pipeline mask, which is used for Method B, is also inaccurate, increasing the contamination from background stars and therefore further increasing the noise.

As the scaling relations of mass, radius and log g are estimates, we note that they are within expected variation. The resulting scaled parameters are expected to be within 2-3% accuracy [Chaplin and Miglio, 2013]. S2016 also includes other methods of finding mass, radius and surface gravity, but we only include their results from scaling relations. S2016 also performs 'Super-Nyquist' analysis on frequencies greater than approximately 283 μHz, which was developed by Yu et al. [2016]. We do not perform this analysis and hence not that the 211403248, 211415364, 211411922, 211409088 and 211414203 may not have an accurate ν_{max}.

3.3. Resulting parameters

Table 3.1: Parameters estimated for each star in M67, these were calculated using the light curves reduced using Method A.

Method A					
K2 ID	$\nu_{max}(\mu Hz)$	$\Delta\nu(\mu Hz)$	Mass ($M_\odot$)	Radius ($R_\odot$)	log g
211413623	60.50	6.48	1.04	7.68	2.69
211396385	74.50	7.06	1.43	8.05	2.78
211414300	82.50	7.70	1.33	7.42	2.82
211408346	93.50	11.32	0.42	3.90	2.88
211410231	107.50	8.88	1.72	7.36	2.94
211412928	122.50	9.78	1.73	6.90	3.00
211411629	204.50	21.80	0.32	2.32	3.22
211414687	233.50	17.76	0.69	3.42	3.21
211416749	199.50	18.28	0.99	3.79	3.28
211421954	249.50	18.81	1.09	3.83	3.31
211409560	269.50	20.21	1.04	3.60	3.34
211388537	266.50	26.85	0.33	2.03	3.34
211403248	131.50	14.53	0.46	3.41	3.03
211415364	185.50	12.82	2.11	6.61	3.18
211411922	251.50	22.93	0.55	2.67	3.32
211409088	226.50	17.95	1.04	3.89	3.27
211414203	174.50	17.96	0.49	3.03	3.17

Table 3.2: Parameters estimated for each star in M67, these were calculated using the light curves reduced using Method B.

Method B					
K2 ID	$\nu_{max}(\mu Hz)$	$\Delta\nu(\mu Hz)$	Mass ($M_\odot$)	Radius ($R_\odot$)	log g
211413623	203.5	19.52	0.48	2.85	3.21
211396385	77.5	6.98	1.68	8.57	2.80
211414300	178.5	19.17	0.35	2.59	3.16
211408346	95.5	8.23	1.59	7.54	2.88
211410231	225.5	15.44	1.74	5.11	3.26
211412928	224.5	18.25	0.88	3.64	3.26
211411629	94.5	9.77	0.79	5.33	2.88
211414687	210.5	15.30	1.48	4.87	3.23
211416749	229.5	16.89	1.29	4.36	3.27
211421954	237.5	17.05	1.40	4.44	3.29
211409560	203.5	17.66	0.77	3.55	3.22
211388537	191.5	14.25	1.56	5.19	3.20
211403248	196.5	13.94	1.81	5.54	3.21
211415364	49.5	6.52	0.60	6.36	2.61
211411922	94.5	11.94	0.40	3.70	2.90
211409088	131.5	12.55	0.85	4.61	3.04
211414203	91.5	9.61	0.86	5.54	2.89

3.3. Resulting parameters

Table 3.3: Seismic parameters as found by S2016 [Stello et al., 2016]

K2 ID	$\nu_{max}(\mu Hz)$	$\Delta\nu(\mu Hz)$	$T_{eff}(K)$	Mass ($M_\odot$)	Radius ($R_\odot$)	log g
211413623	64.84	6.28	4702	1.46	8.77	2.715
211396385	77.4	7.00	4808	1.65	8.50	2.80
211414300	78.8	7.19	4709	1.52	8.12	2.80
211408346	98.7	8.17	4723	1.80	7.90	2.89
211410231	103.1	8.87	4803	1.53	7.08	2.92
211412928	117.8	9.74	4817	1.57	6.70	2.97
211411629	196	14.43	-	-	-	-
211414687	203.0	15.10	4850	1.40	4.82	3.21
211416749	234.3	16.76	4851	1.41	4.51	3.28
211421954	246.1	17.47	4889	1.41	4.38	3.30
211409560	272.2	19.10	4908	1.34	4.06	3.34
211388537	287.6	20.15	5015	1.32	3.90	3.37
211403248	305.5	21.45	4963	1.21	3.64	3.40
211415364	463	28.29	4940	1.39	3.16	3.58
211411922	559	36.34	5158	0.96	2.36	3.67
211409088	562	33.02	5060	1.38	2.85	3.66
211414203	663	46.35	5190	0.61	1.79	3.75

Table 3.4: Parameters estimated for each star in R147, these were calculated using the light curves reduced using Method A

Method A					
K2 ID	$\nu_{max}(\mu Hz)$	$\Delta\nu(\mu Hz)$	Mass ($M_\odot$)	Radius ($R_\odot$)	log g
219310397	246.50	19.99	0.80	3.32	3.30
219403368	87.50	8.99	0.88	5.83	2.85
219624547	175.50	15.21	0.87	4.09	3.15
219688088	57.50	7.26	0.59	5.88	2.67
219697419	56.50	7.11	0.60	6.01	2.66
219704882	112.50	10.00	1.22	6.06	2.96
219757320	85.50	11.02	0.36	3.79	2.84

Table 3.5: Parameters estimated for each star in R147, these were calculated using the light curves reduced using Method B

Method B					
K2 ID	$\nu_{max}(\mu Hz)$	$\Delta\nu(\mu Hz)$	Mass ($M_\odot$)	Radius ($R_\odot$)	log g
219310397	46.5	4.71	1.75	11.28	2.58
219403368	142.5	13.82	0.68	4.02	3.06
219624547	50.5	5.14	1.58	10.30	2.61
219688088	154.5	17.09	0.37	2.85	3.10
219697419	151.5	15.95	0.46	3.21	3.09
219704882	49.5	4.71	2.11	12.01	2.60
219757320	38.5	5.57	0.51	6.68	2.49

In summary of the asteroseismic analysis, the results obtained show that the RGs in M67 and R147 are ideal targets for inclination angle analysis. Most of the RGs have a $\nu_{max} \geq 50\mu Hz$, which is a requirement for this analysis. This analysis also requires detectable rotationally split mixed modes. Even with appended light curves from all observed campaigns (for each star), the noise due to the loss of fine pointing is too

great to identify the individual modes. We find that K2 does not have the frequency resolution to identify mixed modes, this is also confirmed by Stello et al. [2017]. Kamiaka et al. [2018] also find that if a power spectrum that has a low Signal-to-Noise ratio over-estimates low inclination angles and underestimates high inclination angles. The publication also suggests that if inclination angles are to be determined using asteroseismology, the estimation of $v\,sin\,i$, which is done by modelling macroturbulence should be done carefully.

Chapter 4

Conclusion

This thesis contains an analysis of open clusters to show that asteroseismological techniques provide promising results in studying star formation. We selected three open clusters, M67, R147 and NGC 2158, based on their known age (more than one gigayears old) and K2 data availability. Using data from Gaia, we analysed the stellar membership of the clusters by assigning each star in the field of view a kinematic and distance probability. The distance probability ($P_{distance}$) was calculated using literature values for the distance of the clusters. The kinematic probability (P_{Kin}) was calculated using methods from Kharchenko et al. [2012], which uses proper motions of the star and mean proper motion of the cluster to determine whether a star belongs to the cluster or not. The field of view for each cluster was 1.5 times the estimated apparent size by other publications; for M67: 40.5', for R147: 1.875° and for NGC 2158: 12.6'. The total probability was calculated by determining $P_{distance} \times P_{Kin}$. If the star was within 2 standard deviations, it was considered to be a member of the cluster. We find a total of: 540 members for M67 of which 29 are RGs, 92 members for R147 of which 7 are RGs, and 338 members for NGC 2158 of which 11 are RGs.

Following the membership analysis, K2 light curves and target pixel files for all RGs were downloaded. We used two methods to process the light curves. Method A consisted of using targets with a source specific mask, to obtain a light curve for each RG. Then this light curve was de-trended for the 8 most common trends from the observation campaigns. Method B used light curves made using PDC flux (pre-processed

by the *Kepler* pipeline) which had already been de-trended and did not require any other processing. The light curves from both methods did need to be corrected for systematic errors; this was done using the Self-Flat Fielding technique developed by Vanderburg and Johnson [2014]. After the processing was complete we use peak bagging to extract asteroseismological parameters from the stars. Peak bagging involved obtaining a periodogram of light curves, which was then fitted to amplify the astrophysical signal peaks. This fitting was done using the 'Boxkernal' method. The new 'smoothed' periodogram was then used to extract maximum frequency (ν_{max} and the large separation frequency ($\Delta\nu$). Once they were calculated, we used scaling relations to obtain mass, radius and surface gravity for each star. The smoothed periodogram showed that the frequency resolution for K2 is not precise enough to resolve multiple modes for the RGs. Hence this cannot be used to find the inclination angles.

The next step to continue this analysis would be to investigate data from TESS. High precision observations of M67 and R147 would provide an opportunity for not only spin alignment analysis but also other star formation studies. With high precision Gaia data, inclination angles can also be calculated using the Line-Of-Sight velocities and be compared with asteroseismological investigations to confirm accuracy. We find that M67 and R147 are optimal targets to study cluster dynamics because of their rich RG membership. We also find with correct data and processing asteroseismology can be a powerful tool in studying star formation.

Bibliography

Conny Aerts, Jørgen Christensen-Dalsgaard, and Donald W Kurtz. *Asteroseismology*. Springer Science & Business Media, 2010.

European Space Agency. Gaia summary, 2019. URL `https://sci.esa.int/web/gaia/-/28820-summary`.

Pau Amaro-Seoane, Symeon Konstantinidis, Patrick Brem, and Márcio Catelan. Mergers of multimetallic globular clusters: the role of dynamics. *Monthly Notices of the Royal Astronomical Society*, 435(1):809–821, 2013.

H Arp and James Cuffey. The star cluster ngc 2158. *The Astrophysical Journal*, 136: 51, 1962.

Carine Babusiaux, Floor van Leeuwen, MA Barstow, C Jordi, A Vallenari, D Bossini, A Bressan, T Cantat-Gaudin, M Van Leeuwen, AGA Brown, et al. Gaia data release 2-observational hertzsprung-russell diagrams. *Astronomy & astrophysics*, 616:A10, 2018.

Javier Ballesteros-Paredes, Ralf S Klessen, and Enrique Vázquez-Semadeni. Dynamic cores in hydrostatic disguise. *The Astrophysical Journal*, 592(1):188, 2003.

Javier Ballesteros-Paredes, Ralf S Klessen, M-M Mac Low, and Enrique Vázquez-Semadeni. Molecular cloud turbulence and star formation. *arXiv preprint astro-ph/0603357*, 2006.

Geert Barentsen. Kepler and k2 data processing pipeline, October 2019. URL `https://keplerscience.arc.nasa.gov/pipeline.html`.

Geert Barentsen et al. Charecteristics of the kepler space telescope, 2019. URL `https://keplerscience.arc.nasa.gov/the-kepler-space-telescope.html`.

Sydney A Barnes, Joerg Weingrill, Dario Fritzewski, Klaus G Strassmeier, and Imants Platais. Rotation periods for cool stars in the 4 gyr old open cluster m67, the solar–stellar connection, and the applicability of gyrochronology to at least solar age. *The Astrophysical Journal*, 823(1):16, 2016.

Paul G Beck, Josefina Montalban, Thomas Kallinger, Joris De Ridder, Conny Aerts, Rafael A García, Saskia Hekker, Marc-Antoine Dupret, Benoit Mosser, Patrick Eggenberger, et al. Fast core rotation in red-giant stars as revealed by gravity-dominated mixed modes. *Nature*, 481(7379):55, 2012.

PG Beck, Timothy R Bedding, Benoit Mosser, Dennis Stello, RA Garcia, Thomas Kallinger, Saskia Hekker, Yvonne Elsworth, Søren Frandsen, Fabien Carrier, et al. Kepler detected gravity-mode period spacings in a red giant star. *Science*, 332(6026): 205–205, 2011.

Timothy R Bedding and Hans Kjeldsen. Scaled oscillation frequencies and échelle diagrams as a tool for comparative asteroseismology. *arXiv preprint arXiv:1001.5038*, 2010.

Timothy R Bedding, Benoit Mosser, Daniel Huber, Josefina Montalbán, Paul Beck, Jørgen Christensen-Dalsgaard, Yvonne P Elsworth, Rafael A García, Andrea Miglio, Dennis Stello, et al. Gravity modes as a way to distinguish between hydrogen-and helium-burning red giant stars. *Nature*, 471(7340):608, 2011.

A Bellini, LR Bedin, B Pichardo, E Moreno, C Allen, G Piotto, and J Anderson. Absolute proper motion of the galactic open cluster m 67. *Astronomy & Astrophysics*, 513:A51, 2010.

AGA Brown, A Vallenari, T Prusti, JHJ De Bruijne, C Babusiaux, CAL Bailer-Jones, M Biermann, Dafydd Wyn Evans, L Eyer, Femke Jansen, et al. Gaia data release 2-summary of the contents and survey properties. *Astronomy & astrophysics*, 616: A1, 2018.

Timothy M Brown and Ronald L Gilliland. Asteroseismology. *Annual Review of Astronomy and Astrophysics*, 32(1):37–82, 1994.

Joleen K Carlberg. Rotational and radial velocities of 1.3-2.2 m red giants in open clusters. *The Astronomical Journal*, 147(6):138, 2014.

Giovanni Carraro, Léo Girardi, and Paola Marigo. The intermediate-age open cluster ngc 2158. *Monthly Notices of the Royal Astronomical Society*, 332(3):705–713, 2002.

William J Chaplin and Andrea Miglio. Asteroseismology of solar-type and red-giant stars. *Annual Review of Astronomy and Astrophysics*, 51:353–392, 2013.

Jørgen Christensen-Dalsgaard. Asteroseismology with solar-like oscillations. *Variability of the Sun and Sun-like Stars: from Asteroseismology to Space Weather*, page 125, 2018.

CA Christian, JN Heasley, and KA Janes. The open cluster ngc 2158. *The Astrophysical Journal*, 299:683–694, 1985.

JL Christiansen, JE Van Cleve, JM Jenkins, DA Caldwell, T Barclay, S Bryson, CJ Burke, JD Twicken, and AK Uddin. Kepler data characteristics handbook. *KSCI-19040*, 2013.

Enrico Corsaro, Yueh-Ning Lee, Rafael A García, Patrick Hennebelle, Savita Mathur, Paul G Beck, Stephane Mathis, Dennis Stello, and Jérôme Bouvier. Formation history of open clusters constrained by detailed asteroseismology of red giant stars observed by kepler. In *EPJ Web of Conferences*, volume 160, page 05002. EDP Sciences, 2017.

Jason L Curtis, Angie Wolfgang, Jason T Wright, John M Brewer, and John Asher Johnson. Ruprecht 147: The oldest nearby open cluster as a new benchmark for stellar astrophysics. *The Astronomical Journal*, 145(5):134, 2013.

Joris De Ridder, Caroline Barban, Frédéric Baudin, Fabien Carrier, Artie P Hatzes, Saskia Hekker, Thomas Kallinger, Werner W Weiss, Annie Baglin, Michel Auvergne, et al. Non-radial oscillation modes with long lifetimes in giant stars. *Nature*, 459 (7245):398, 2009.

Wilton S Dias, M Assafin, V Flório, BS Alessi, and V Líbero. Proper motion determination of open clusters based on the ucac2 catalogue. *Astronomy & Astrophysics*, 446(3):949–953, 2006.

RL Dickman and SC Kleiner. Largescale structure of the taurus molecular complex-part three-methods for turbulence. *The Astrophysical Journal*, 295:479, 1985.

European Space Association. Payload module, 2013. URL `http://sci.esa.int/gaia/40129-payload-module/?fbodylongid=1906`. Online; accessed 23 July 2019.

Aaron M Geller, David W Latham, and Robert D Mathieu. Stellar radial velocities in the old open cluster m67 (ngc 2682). i. memberships, binaries, and kinematics. *The Astronomical Journal*, 150(3):97, 2015.

Laurent Gizon and SK Solanki. Determining the inclination of the rotation axis of a sun-like star. *The Astrophysical Journal*, 589(2):1009, 2003.

Raffaele Gratton, Christopher Sneden, and Eugenio Carretta. Abundance variations within globular clusters. *Annu. Rev. Astron. Astrophys.*, 42:385–440, 2004.

Gerald Handler. Asteroseismology. *Planets, Stars and Stellar Systems: Volume 4: Stellar Structure and Evolution*, pages 207–241, 2013.

Jarrod R Hurley, Onno R Pols, Sverre J Aarseth, and Christopher A Tout. A complete n-body model of the old open cluster m67. *Monthly Notices of the Royal Astronomical Society*, 363(1):293–314, 2005.

JH Jeans. Astronomy and cosmology, cambridge univ. *P ress*, 1(9):2, 1929.

Mathis John. Molecular cloud, 2009. URL `https://www.britannica.com/science/molecular-cloud`.

Michele Johnson. Kepler's second light: How k2 will work, August 2017. URL `https://www.nasa.gov/kepler/keplers-second-light-how-k2-will-work`.

Eric Jones, Travis Oliphant, Pearu Peterson, et al. SciPy: Open source scientific tools for Python, 2001. URL `http://www.scipy.org/`.

Sebastian Kamann, NJ Bastian, Mark Gieles, Eduardo Balbinot, and Vincent Hénault-Brunet. Linking the rotation of a cluster to the spins of its stars: the kinematics of ngc 6791 and ngc 6819 in 3d. *Monthly Notices of the Royal Astronomical Society*, 483(2):2197–2206, 2018.

Shoya Kamiaka, Othman Benomar, and Yasushi Suto. Reliability of stellar inclination estimated from asteroseismology: analytical criteria, mock simulations, and kepler data analysis. *Monthly Notices of the Royal Astronomical Society*, 479(1):391–405, 2018.

N Kharchenko, V Andruk, and E Schilbach. Schmidt survey in the galactic anticentre direction. 1. investigation of open clusters. *Astronomische Nachrichten*, 318(5):253–266, 1997.

NV Kharchenko, AE Piskunov, S Röser, E Schilbach, and R-D Scholz. 109 new galactic open clusters. *Astronomy & Astrophysics*, 440(1):403–408, 2005a.

NV Kharchenko, AE Piskunov, S Röser, E Schilbach, and R-D Scholz. Astrophysical parameters of galactic open clusters. *Astronomy & Astrophysics*, 438(3):1163–1173, 2005b.

NV Kharchenko, AE Piskunov, E Schilbach, S Röser, and R-D Scholz. Global survey of star clusters in the milky way-i. the pipeline and fundamental parameters in the second quadrant. *Astronomy & Astrophysics*, 543:A156, 2012.

NV Kharchenko, AE Piskunov, E Schilbach, S Röser, and R-D Scholz. Global survey of star clusters in the milky way-ii. the catalogue of basic parameters. *Astronomy & Astrophysics*, 558:A53, 2013.

K Kinemuchi, T Barclay, M Fanelli, J Pepper, M Still, and Steve B Howell. Demystifying kepler data: A primer for systematic artifact mitigation. *Publications of the Astronomical Society of the Pacific*, 124(919):963, 2012.

Ivan King. The structure of star clusters. i. an empirical density law. *The Astronomical Journal*, 67:471, 1962.

Rudolf Kippenhahn, Alfred Weigert, and Achim Weiss. *Stellar structure and evolution*, volume 192. Springer, 1990.

Charles J Lada and Nikolaos D Kylafis. *The Origin of Stars and Planetary Systems*, volume 540. Springer Science & Business Media, 2012a.

Charles J Lada and Nikolaos D Kylafis. *The Physics of Star Formation and Early Stellar Evolution*, volume 342. Springer Science & Business Media, 2012b.

Charles J Lada and Elizabeth A Lada. Embedded clusters in molecular clouds. *Annual Review of Astronomy and Astrophysics*, 41(1):57–115, 2003.

Richard B Larson. Turbulence and star formation in molecular clouds. *Monthly Notices of the Royal Astronomical Society*, 194(4):809–826, 1981.

Richard B Larson. The physics of star formation. *Reports on Progress in Physics*, 66 (10):1651, 2003.

Lightkurve Collaboration, J. V. d. M. Cardoso, C. Hedges, M. Gully-Santiago, N. Saunders, A. M. Cody, T. Barclay, O. Hall, S. Sagear, E. Turtelboom, J. Zhang, A. Tzanidakis, K. Mighell, J. Coughlin, K. Bell, Z. Berta-Thompson, P. Williams, J. Dotson, and G. Barentsen. Lightkurve: Kepler and TESS time series analysis in Python. Astrophysics Source Code Library, December 2018.

L Lindegren, J Hernandez, A Bombrun, S Klioner, U Bastian, M Ramos-Lerate, A De Torres, H Steidelmüller, C Stephenson, D Hobbs, et al. Gaia data release 2-the astrometric solution. *Astronomy & Astrophysics*, 616:A2, 2018.

Steven Majewskki. Stellar motions, 2018.

Christopher D Matzner. On the role of massive stars in the support and destruction of giant molecular clouds. *The Astrophysical Journal*, 566(1):302, 2002.

Christopher F McKee and Eve C Ostriker. Theory of star formation. *Annu. Rev. Astron. Astrophys.*, 45:565–687, 2007.

PC Myers. Dense cores in dark clouds. iii-subsonic turbulence. *the Astrophysical Journal*, 270:105–118, 1983.

François Ochsenbein, Patricia Bauer, and James Marcout. The vizier database of astronomical catalogues. *Astronomy and Astrophysics Supplement Series*, 143(1): 23–32, 2000.

M Sally Oey and CJ Clarke. Statistical confirmation of a stellar upper mass limit. *The Astrophysical Journal Letters*, 620(1):L43, 2005.

Giampaolo Piotto. Observations of multiple populations in star clusters. *Proceedings of the International Astronomical Union*, 4(S258):233–244, 2008.

AE Piskunov, E Schilbach, NV Kharchenko, S Röser, and R-D Scholz. Towards absolute scales for the radii and masses of open clusters. *Astronomy & Astrophysics*, 468 (1):151–161, 2007.

Svein Rosseland and Gunnar Randers. On the stability of pulsating stars. *Astrophysica Norvegica*, 3:71, 1938.

Dennis Stello, Daniel Huber, Sanjib Sharma, Jennifer Johnson, Mikkel N Lund, Rasmus Handberg, Derek L Buzasi, Victor Silva Aguirre, William J Chaplin, Andrea Miglio, et al. Oscillating red giants observed during campaign 1 of the kepler k2 mission: new prospects for galactic archaeology. *The Astrophysical Journal Letters*, 809(1): L3, 2015.

Dennis Stello, Andrew Vanderburg, Luca Casagrande, Ron Gilliland, Victor Silva Aguirre, Eric Sandquist, Emily Leiner, Robert Mathieu, and David R Soderblom. The k2 m67 study: Revisiting old friends with k2 reveals oscillating red giants in the open cluster m67. *The Astrophysical Journal*, 832(2):133, 2016.

Dennis Stello, Joel Zinn, Yvonne Elsworth, Rafael A Garcia, Thomas Kallinger, Savita Mathur, Benoit Mosser, Sanjib Sharma, William J Chaplin, Guy Davies, et al. The k2 galactic archaeology program data release i: Asteroseismic results from campaign 1. *The Astrophysical Journal*, 835(1):83, 2017.

Guillermo Torres, Jason L Curtis, Andrew Vanderburg, Adam L Kraus, and Aaron Rizzuto. Eclipsing binaries in the open cluster ruprecht 147. i. epic 219394517. *The Astrophysical Journal*, 866(1):67, 2018.

Andrew Vanderburg and John Asher Johnson. A technique for extracting highly precise photometry for the two-wheeled kepler mission. *Publications of the Astronomical Society of the Pacific*, 126(944):948, 2014.

Lucas S Viani, Sarbani Basu, Enrico Corsaro, Warrick H Ball, and William J Chaplin. Determining the best method of calculating the large frequency separation for stellar models. *arXiv preprint arXiv:1905.08333*, 2019.

Mike Wall. Nasa's hobbled planet-hunting spacecraft may resume search for alien worlds, 2013. URL `https://www.space.com/23465-planet-hunting-kepler-spacecraft-future.html`.

Fu Chi Yeh, Giovanni Carraro, Marco Montalto, and Anton F Seleznev. Ruprecht 147: a paradigm of dissolving star cluster. *The Astronomical Journal*, 157(3):115, 2019.

Jie Yu, Daniel Huber, Timothy R Bedding, Dennis Stello, Simon J Murphy, Maosheng Xiang, Shaolan Bi, and Tanda Li. Asteroseismology of 1523 misclassified red giants using kepler data. *Monthly Notices of the Royal Astronomical Society*, 463(2):1297–1306, 2016.